



RESEARCH ARTICLE

10.1029/2022SW003215

Special Section:

Understanding the interconnected sun-heliospheric-planetary system during solar minimum

Key Points:

- We analyze the eruption and propagation of two coronal mass ejections (CMEs) from the Sun up to Earth and Mars during August 2018
- Both CMEs were observed at Earth, but the second missed Mars, possibly due to interaction with a following high-speed solar wind stream
- The sequence of events observed resulted in a strong magnetic storm at Earth, but only moderate disturbances at Mars

Supporting Information:

Supporting Information may be found in the online version of this article.

Correspondence to:

E. Palmerio,
epalmerio@predsci.com

Citation:

Palmerio, E., Lee, C. O., Richardson, I. G., Nieves-Chinchilla, T., Dos Santos, L. F. G., Gruesbeck, J. R., et al. (2022). CME evolution in the structured heliosphere and effects at Earth and Mars during solar minimum. *Space Weather*, 20, e2022SW003215. <https://doi.org/10.1029/2022SW003215>

Received 11 JUL 2022
Accepted 12 SEP 2022

CME Evolution in the Structured Heliosphere and Effects at Earth and Mars During Solar Minimum

Erika Palmerio^{1,2,3} , Christina O. Lee² , Ian G. Richardson^{4,5} , Teresa Nieves-Chinchilla⁵ , Luiz F. G. Dos Santos⁶ , Jacob R. Gruesbeck⁷ , Nariaki V. Nitta⁸ , M. Leila Mays⁵ , Jasper S. Halekas⁹ , Cary Zeitlin¹⁰ , Shaosui Xu² , Mats Holmström¹¹ , Yoshifumi Futaana¹¹ , Tamitha Mulligan^{12,13} , Benjamin J. Lynch² , and Janet G. Luhmann² 

¹Predictive Science Inc., San Diego, CA, USA, ²Space Sciences Laboratory, University of California–Berkeley, Berkeley, CA, USA, ³CPAESS, University Corporation for Atmospheric Research, Boulder, CO, USA, ⁴Department of Astronomy, University of Maryland, College Park, MD, USA, ⁵Heliospheric Physics Division, NASA Goddard Space Flight Center, Greenbelt, MD, USA, ⁶NextSource Inc., New York, NY, USA, ⁷Solar System Exploration Division, NASA Goddard Space Flight Center, Greenbelt, MD, USA, ⁸Lockheed Martin Solar and Astrophysics Laboratory, Palo Alto, CA, USA, ⁹Department of Physics and Astronomy, University of Iowa, Iowa City, IA, USA, ¹⁰Leidos Innovations Corporation, Houston, TX, USA, ¹¹Swedish Institute of Space Physics, Kiruna, Sweden, ¹²Space Sciences Department, The Aerospace Corporation, Los Angeles, CA, USA, ¹³Department of Earth Sciences, Millersville University, Millersville, PA, USA

Abstract The activity of the Sun alternates between a solar minimum and a solar maximum, the former corresponding to a period of “quieter” status of the heliosphere. During solar minimum, it is in principle more straightforward to follow eruptive events and solar wind structures from their birth at the Sun throughout their interplanetary journey. In this paper, we report analysis of the origin, evolution, and heliospheric impact of a series of solar transient events that took place during the second half of August 2018, that is, in the midst of the late declining phase of Solar Cycle 24. In particular, we focus on two successive coronal mass ejections (CMEs) and a following high-speed stream (HSS) on their way toward Earth and Mars. We find that the first CME impacted both planets, whilst the second caused a strong magnetic storm at Earth and went on to miss Mars, which nevertheless experienced space weather effects from the stream interacting region preceding the HSS. Analysis of remote-sensing and in-situ data supported by heliospheric modeling suggests that CME–HSS interaction resulted in the second CME rotating and deflecting in interplanetary space, highlighting that accurately reproducing the ambient solar wind is crucial even during “simpler” solar minimum periods. Lastly, we discuss the upstream solar wind conditions and transient structures responsible for driving space weather effects at Earth and Mars.

Plain Language Summary The Sun is characterized by a 11-year periodicity of its levels of activity, resulting in a solar minimum and a solar maximum alternating approximately every 5.5 years. During solar minimum, the Sun and its whole environment are in their simplest configuration, and eruptive events are significantly less frequent. It follows that periods of lower activity are generally considered optimal for tracking solar phenomena from their origin at the Sun throughout their journey in interplanetary space. In this paper, we analyze a series of solar eruptions that took place during the second half of August 2018 and follow them until their arrival at Earth and Mars, taking into account their associated effects on the two planets. We find that, even during solar minimum, the large-scale structure of the solar and interplanetary environment can have more or less dramatic impacts on the evolution of eruptions as they travel away from the Sun. Additionally, we suggest that the same event can cause diverse levels of disturbances at different planets, depending on the particular structure and properties of the impacting solar wind.

1. Introduction

The solar activity is characterized by numerous short- and long-term periodicities, the most renowned of which is the 11-year solar magnetic activity cycle (Hathaway, 2015). Over the duration of a full cycle, the number of sunspots as well as the fraction of solar surface covered by them rise until reaching a maximum and then fall again. This trend is also followed by the occurrence of solar eruptions, including flares (e.g., Benz, 2017) and coronal mass ejections (CMES; e.g., Webb & Howard, 2012), which tend to peak close to solar maximum and decrease drastically around solar minimum. Due to the general lack of active regions, CMEs during solar minimum tend to

© 2022. The Authors.

This is an open access article under the terms of the [Creative Commons Attribution License](https://creativecommons.org/licenses/by/4.0/), which permits use, distribution and reproduction in any medium, provided the original work is properly cited.

be of the slow, streamer-blowout kind (e.g., Vourlidas & Webb, 2018), although some major active-region eruptions may still occur (e.g., Nitta, 2011). Solar minimum periods are characterized by a simpler configuration of the solar magnetic field, a generally slower and less variable solar wind, and a less energized space environment (Riley et al., 2001, 2022). These aspects make minima excellent times for tracing solar phenomena “from start to finish” and for defining the baseline heliophysical system, giving rise to large, coordinated initiatives such as the Whole Sun Month (WSM; Galvin & Kohl, 1999), which took place during the cycle 22–23 minimum, and the Whole Heliosphere Interval (WHI; Thompson et al., 2011), which took place during the cycle 23–24 minimum. CME occurrence usually drops to about one per week, meaning that CME–CME interactions tend to be significantly less likely and that it is possible to follow the evolution of single CMEs and their interaction with solar wind structures, including the slow wind, high-speed streams (HSSs), and slow–fast stream interaction regions (SIRs; e.g., Richardson, 2018).

During the cycle 24–25 minimum, the availability of space- and ground-based assets at various planets or scattered throughout the heliosphere, together with the growing consensus about the importance of multi-point studies within the heliosphere as a whole, have led to the establishment of an even more comprehensive follow-up effort to WSM and WHI, that is, the Whole Heliosphere and Planetary Interactions (WHPI; <https://whpi.hao.ucar.edu/>) initiative, which aims to study the interconnected solar–heliospheric–planetary system. In particular, a relatively large fleet of instruments was and is still operational at Mars, providing us with the opportunity to follow solar transients from the Sun to Earth and/or Mars and to characterize their space weather response at the two planets. Occasionally, the same transient may even encounter both Earth and Mars and elicit dissimilar impacts at each planet. Earth is characterized by a strong intrinsic quasi-dipolar magnetic field that is able to sustain a full-fledged magnetosphere (e.g., Pulkkinen, 2007). Since Earth's field is roughly directed toward the North in the equatorial plane at the magnetopause, the most geoeffective solar wind structures are those containing southward magnetic field (Zhang et al., 2007) as well as high speed and ram pressure (Gonzalez et al., 1994). Mars, on the other hand, lacks a global magnetic dipole and interaction between the solar wind and the Martian ionosphere generates a so-called induced magnetosphere (e.g., Bertucci et al., 2011), which however differs from a Venus- or comet-like one due to the presence of localized crustal magnetic fields (Acuna et al., 1998), thus leading to a “hybrid” magnetosphere (e.g., DiBraccio et al., 2018). As a result, the main parameters that regulate the *arieffectiveness*—from the Greek name for Mars, *Ἄρης* or *Áris*—of a solar wind transient are the dynamic pressure (Opengoorth et al., 2013), usually enhanced in CMEs and SIRs, and the topology of the interplanetary magnetic field (Jakosky, Grebowsky, et al., 2015).

Despite the recent increasing interest in space weather at Mars (e.g., Geyer et al., 2021; Huang et al., 2021; Lee et al., 2017; Luhmann et al., 2017; Zhao et al., 2021), most studies have focused on the analysis of the consequences of large and clear solar events (e.g., Crider et al., 2005; Jakosky, Grebowsky, et al., 2015; Lee et al., 2018), whilst less is known about minor events observed during periods of low solar activity (e.g., Kajdič et al., 2021; Sánchez-Cano et al., 2017). In order to tackle this issue, we present in this article a detailed analysis of a sequence of solar transients during the second half of August 2018 (i.e., during the late declining phase of Solar Cycle 24) between Earth and Mars, which were separated by $\sim 8^\circ$ in longitude, $\sim 2^\circ$ in latitude, and ~ 0.4 AU in radial distance. Some aspects of these events were addressed by a number of studies (e.g., Abunin et al., 2020; Akala et al., 2021; Chen et al., 2019; Cherniak & Zakharenkova, 2022; Gopalswamy et al., 2022; Mishra & Srivastava, 2019; Moro et al., 2022; Nitta et al., 2021; Piersanti et al., 2020; Thampi et al., 2021; Younas et al., 2020; Zhang et al., 2020), and our goal here is to provide a holistic Sun-to-Mars investigation of their evolution from the Sun through the inner heliosphere and their effects at the two planets. Accordingly, we first present remote-sensing observations of the eruptive events. Then, we summarize the heliospheric context necessary to interpret in-situ observations at Earth and Mars. Then, we show solar wind and interplanetary magnetic field measurements at the two planets, with particular attention to the space weather responses to the interplanetary disturbances. Finally, we discuss these observations within the larger context of terrestrial and martian space weather during solar minimum periods.

2. Remote-Sensing Observations

The 20 August 2018 eruptive events were observed in remote-sensing imagery from two vantage points, namely Earth and the Solar Terrestrial Relations Observatory Ahead (STEREO-A; Kaiser et al., 2008) spacecraft, located $\sim 110^\circ$ east of Earth close to 1 AU. Here, we provide an overview of the sequence of events from their origin

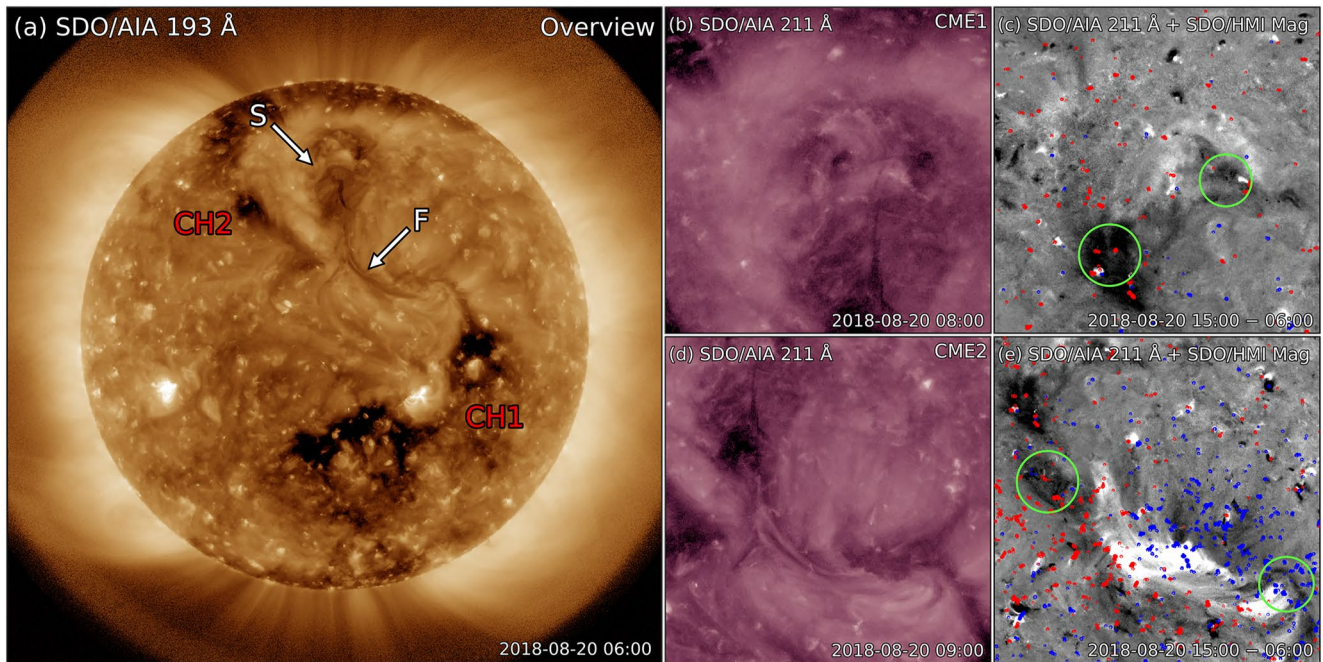


Figure 1. Overview of the 2018 August 20 eruptions from remote-sensing solar disc imagery. (a) Pre-eruptive configuration on the solar disc. The erupting S-shaped structure (“S”) and filament (“F”), as well as the two nearby coronal holes (“CH1” and “CH2”) are labeled. (b) and (d) Zoomed-in images of the erupting sigmoid (CME1) and filament (CME2), respectively. (c) and (e) Base-difference images of the sigmoid and filament eruptions, respectively, with magnetogram data saturated to ± 100 G overlaid (red = positive, blue = negative). The approximate eruption footprints are indicated with green circles in both panels.

at the Sun (Section 2.1) through their evolution across the solar corona (Section 2.2) and inner heliosphere (Section 2.3).

2.1. Solar Disc

The sequence of eruptive events analyzed in this study commenced on 20 August 2018 from an extended quiet-Sun region in the northern hemisphere located close to the central meridian from Earth’s perspective. Figure 1a shows the pre-eruptive configuration in extreme ultra-violet (EUV) at 193 Å as seen by the Atmospheric Imaging Assembly (AIA; Lemen et al., 2012) onboard the Solar Dynamics Observatory (SDO; Pesnell et al., 2012) in orbit around Earth. The most striking features that were present on the Earth-facing Sun are an extended filament channel (marked as “F”) and two coronal holes (CHs), a large one to the southwest of the filament (marked as “CH1”) and a smaller one to the northeast (marked as “CH2”). Additionally, we note an S-shaped feature to the north of the filament (marked as “S”), reminiscent of a sigmoid (e.g., Green et al., 2007)—this structure is visible in several SDO/AIA channels, including 94 Å and 131 Å, which are known to respond to hotter plasma (O’Dwyer et al., 2010).

Both structures (i.e., the S-shaped feature and the filament) began erupting essentially at the same time, around 07:30 UT on 20 August, possibly in a sympathetic fashion (e.g., Lynch & Edmondson, 2013; Török et al., 2011). Whilst the S-shaped structure (Figure 1b) left the Sun rather rapidly (no signatures of the event were visible after a few hours), the filament (Figure 1d) was involved in a much slower eruption, with post-eruption arcades still developing many hours after the onset and into the following day. Therefore, in this work we will define the S-shaped feature eruption as CME1, and the filament eruption as CME2. Around 18:30 UT on 20 August, a small portion of filament lying between the source regions of CME1 and CME2 erupted in a jet-like fashion (see Mishra & Srivastava, 2019, for details)—this may be considered as a “second part” of a two-step filament eruption, as suggested by Abunin et al. (2020). The full sequence of events observed by SDO is shown in EUV at 211 Å in Movie S1 in Supporting Information S1.

Analysis of the pre-eruptive magnetic configuration of the two CMEs (see Palmerio et al., 2017, and references therein) suggests that CME1 was characterized by right-handed chirality (note its forward-S shape), whilst CME2

was left-handed (note its reverse S-shape). The approximate eruption footpoints (estimated via the locations of coronal dimmings; e.g., Reinard & Biesecker, 2009; Thompson et al., 2000) and the magnetic field polarities in which they are rooted are shown in Figure 1c for CME1 and Figure 1e for CME2. Given that CME2 originated from a decayed active region, it is evident that its northeastern (southwestern) footpoint is rooted in a patch of positive (negative) polarity. Thus, its flux rope magnetic configuration upon eruption should be west–south–east (WSE), following the convention of Bothmer and Schwenn (1998) and Mulligan et al. (1998). CME1, on the other hand, originated from a region of much weaker, quiet-Sun magnetic field, making determination of its magnetic structure and orientation more difficult. Nevertheless, the easternmost footpoint seems to be rooted in a patch of positive polarity, which for a right-handed flux rope would result somewhere between a west–north–east (WNE) and a south–west–north (SWN) type.

2.2. Solar Corona

At the time of the 20 August 2018 eruptive events, white-light imagery of the solar corona was available from the Large Angle and Spectrometric Coronagraph (LASCO; Brueckner et al., 1995) onboard the Solar and Heliospheric Observatory (SOHO; Domingo et al., 1995), located at Earth's Lagrange L1 point, as well as the coronagraphs forming part of the Sun Earth Connection Coronal and Heliospheric Investigation (SECCHI; Howard et al., 2008) suite onboard STEREO-A. Given that both CME1 and CME2 originated close to the central meridian as seen from Earth, we expect SOHO to have observed the eruptions approximately along their propagation direction, whilst STEREO-A had a near-quadrature view of the events. Such observations are summarized in Figure 2, and the full sequence of imagery from STEREO/SECCHI/COR2-A and SOHO/LASCO/C2 is provided in Movie S2 and Movie S3 in Supporting Information S1, respectively.

First of all, we note the presence of coronal outflows preceding the eruption(s), indicated in Figures 2a and 2f and possibly associated with blobs originating from the cusp of the helmet streamer belt (e.g., Lynch, 2020; Wang et al., 2000). CME1 first appeared in the COR2-A field of view around 10:24 UT on 20 August (Figures 2a–2c), featuring a rather irregular morphology (it could be classified as a “jet” according to the definition of Vourlidis et al., 2013, 2017). Furthermore, it appeared very faintly in STEREO-A imagery (and is more visible in Movie S2 in Supporting Information S1 than in the still images shown in Figures 2a–2c), likely partially due to the presence of the preceding outflow along the line of sight, and was not clearly discernible in SOHO data (Figures 2e–2g). We note that CME events in the solar corona that appear faint/jet-like from one viewpoint and are not visible at all in another have been reported in previous studies, and may cause moderate geomagnetic disturbances (e.g., Palmerio et al., 2019).

CME2 first appeared in the COR2-A field of view around 13:24 UT on 20 August (Figures 2i–2k) and in the C2 field of view around 21:48 UT on the same day (Figures 2m–2o). This event was significantly more evident than CME1 in images from both perspectives, with a flux rope-like morphology observed by STEREO-A and a full halo (albeit very faint) detected by SOHO. In particular, COR2-A imagery reveals an initially asymmetric structure, with its southern leg ahead of the northern one, that slowly swells before finally accelerating away from the Sun in a streamer-blowout fashion (e.g., Vourlidis & Webb, 2018). As the CME traveled through the solar corona, its front became progressively less asymmetric, possibly indicating that either the northern leg caught up with the southern one, or that the whole structure rotated during its early propagation.

In order to estimate the geometric and kinematic properties of CME1 and CME2 through the solar corona, we fit both eruptions as they appeared in coronagraph imagery with the Graduated Cylindrical Shell (GCS; Thernisien et al., 2006, 2009) model. This will also serve to determine the CME input parameters needed for heliospheric modeling of their propagation through the structured solar wind (see Section 3). The GCS model consists of a parametrized shell (with six free parameters) intended to reproduce the flux rope morphology of CMEs, which can be applied to one or more nearly-simultaneous images and visually adjusted until its projection onto each field of view best matches the observations. Examples of GCS results are shown in the rightmost column of Figure 2, for both CME1 (Figures 2d and 2h) and CME2 (Figures 2l and 2p). Both eruptions are estimated to have a low inclination to the solar equatorial plane in the outer solar corona, and the CME2 results indicate that it is larger (extending $\sim 60^\circ$ vs. $\sim 40^\circ$ along the axis) but slower ($\sim 300 \text{ km s}^{-1}$ vs. $\sim 500 \text{ km s}^{-1}$) than CME1. We remark, however, that the GCS model is applied to single-point (STEREO-A) measurements for CME1 (Figure 2h simply shows the projection of the shell in Figure 2d onto the C2 field of view), inevitably resulting in larger uncertainties. Considering the flux rope types estimated at the Sun (see Section 2.1) and the low inclination

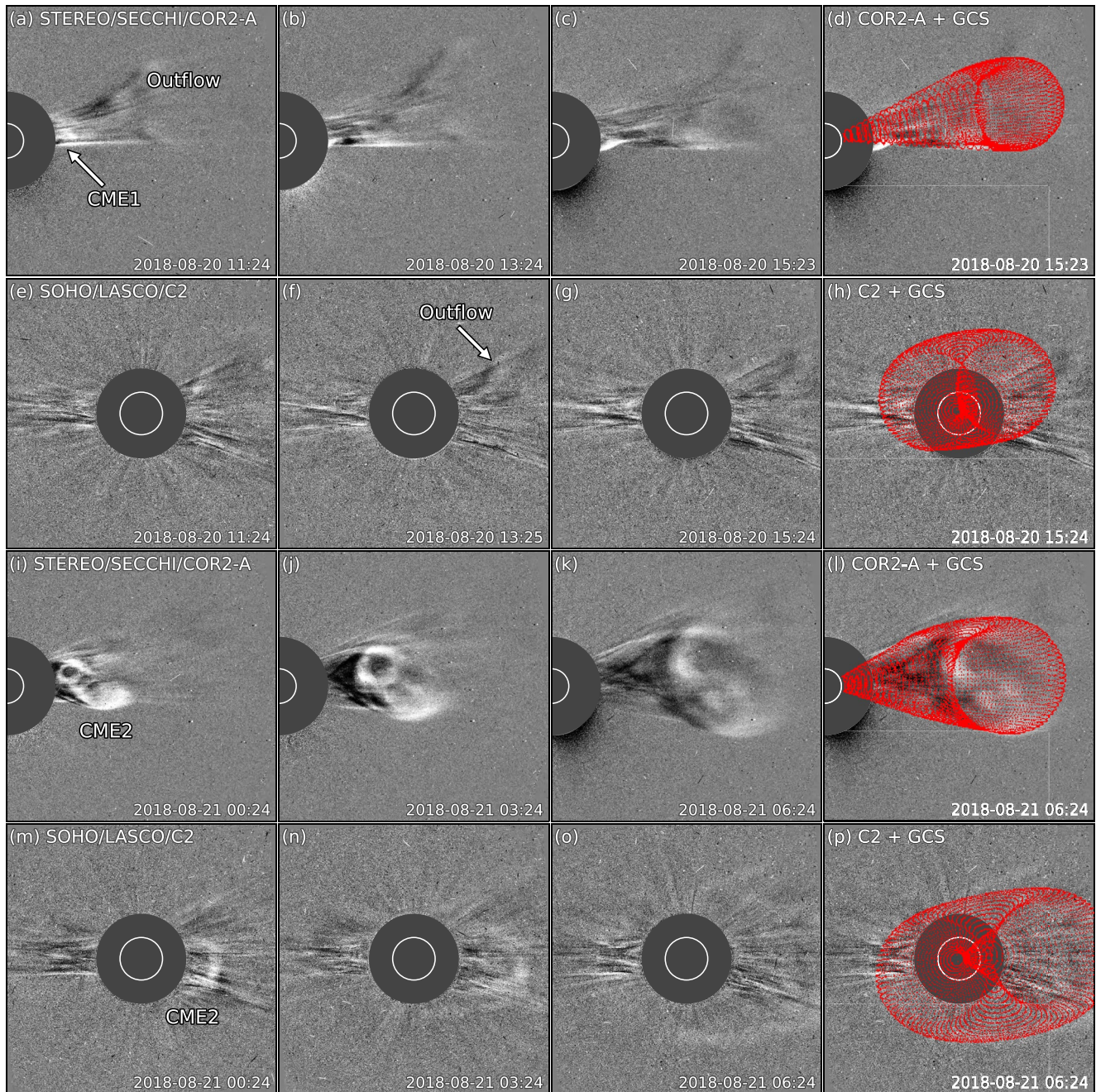


Figure 2. Overview of the 2018 August 20 eruptions from remote-sensing coronagraph imagery (shown here in running difference with $\Delta t = 1$ hr). The first appearances of the preceding outflow, CME1, and CME2 in the field of view each observing instrument are indicated in the respective panels. The rightmost column shows coronagraph images with the Graduated Cylindrical Shell wireframes overlaid, showing the reconstruction of CME1 in panels (d) and (h) and CME2 in panels (l) and (p).

of both eruptions through the solar corona, CME1 is expected to have an SWN configuration, whilst CME2 would reach a north–west–south (NWS) orientation via a counterclockwise rotation of its axis (as expected for left-handed flux ropes, e.g., Green et al., 2007; Lynch et al., 2009).

2.3. Inner Heliosphere

After leaving the COR2-A field of view, the eruptions under analysis were observed by the Heliospheric Imager (HI; Eyles et al., 2009) cameras onboard STEREO-A. Figure 3 shows an overview of the observations of CME1

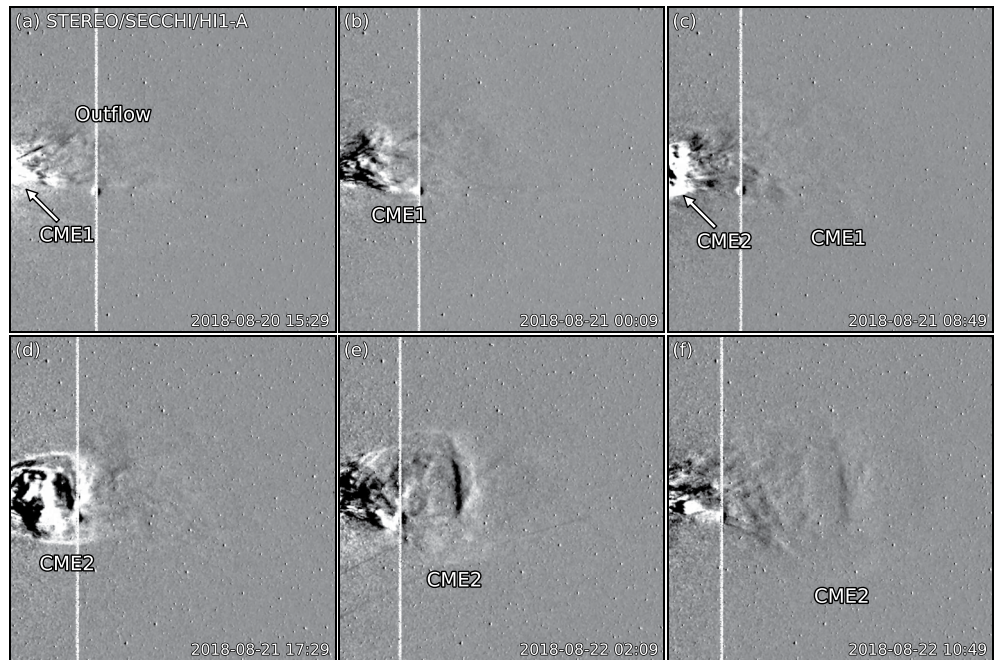


Figure 3. Overview of the 2018 August 20 eruptions from remote-sensing inner heliospheric imagery (shown here in running difference with $\Delta t = 40$ min). The locations of the preceding outflow, CME1, and CME2 are indicated in each panel, where appropriate. The vertical band visible throughout the image sequence is caused by Mercury.

and CME2 through the STEREO/SECCHI/HI1-A camera, whilst the complete set of images is provided in Movie S4 in Supporting Information S1.

CME1 first appeared in the HI1-A field of view at 15:29 UT on 20 August, whilst CME2 emerged at 06:09 UT on 21 August. CME1 maintained a rather irregular morphology, similar to that observed in COR2-A imagery (see Figures 2a–2c and Movie S2 in Supporting Information S1). CME2, on the other hand, displayed a significantly flatter front than the one featured in COR2-A observations (see Figures 2e–2g and Movie S2 in Supporting Information S1), likely due to pancaking, that is, flattening of the CME cross-section as it propagates through a latitudinally-structured ambient wind (e.g., Owens, 2006; Riley & Crooker, 2004). Furthermore, the front of CME1 appeared well ahead of CME2 throughout the sequence of frames in which both eruptions are visible, hence we do not observe signatures of CME–CME interaction in HI1-A imagery.

3. Heliospheric Context

In order to explore the propagation of CME1 and CME2 within their corresponding inner heliospheric context, we employ the Wang–Sheeley–Arge (WSA; Arge et al., 2004) coronal model coupled with the Enlil (Odstroicil, 2003) heliospheric model, hereafter WSA–Enlil. WSA is used to generate the solar wind background from synoptic magnetogram maps (in this case, from the Global Oscillation Network Group or GONG; Harvey et al., 1996), which Enlil takes as input at its inner boundary (set at $21.5 R_{\odot}$ or 0.1 AU). Enlil then models the heliospheric conditions outwards to an outer boundary (in this case set at 2 AU) by solving the magnetohydrodynamic (MHD) equations. CMEs are inserted in WSA–Enlil at the heliospheric inner boundary as hydrodynamic structures, that is, lacking an internal magnetic field. We derive the input parameters for CME1 and CME2 (shown in Table 1) entirely from the GCS reconstructions outlined in Section 2.2 and Figure 2. The latitudes (θ), longitudes (ϕ), and tilts (γ) are taken directly from their values at the last GCS reconstructions before the CMEs left the

Table 1
Coronal Mass Ejection (CME) Input Parameters for the WSA–Enlil Simulation Run

CME #	t_0 (UT)	θ (°)	ϕ (°)	γ (°)	ψ_1 (°)	ψ_2 (°)	V_0 (km s ⁻¹)
1	2018-08-20T18:16	12	2	10	21	12	483
2	2018-08-21T10:56	5	10	9	30	16	290

Note. The table shows, from left to right: CME number, time (t_0) of insertion of the CME at the Enlil inner boundary of $21.5 R_{\odot}$ or 0.1 AU, latitude (θ) and longitude (ϕ) of the CME apex in Stonyhurst coordinates, tilt (γ) of the CME axis with respect to the solar equator (defined positive for counterclockwise rotations), semi-major (ψ_1) and semi-minor (ψ_2) axes of the CME cross-section, and CME speed at $21.5 R_{\odot}$ (V_0).

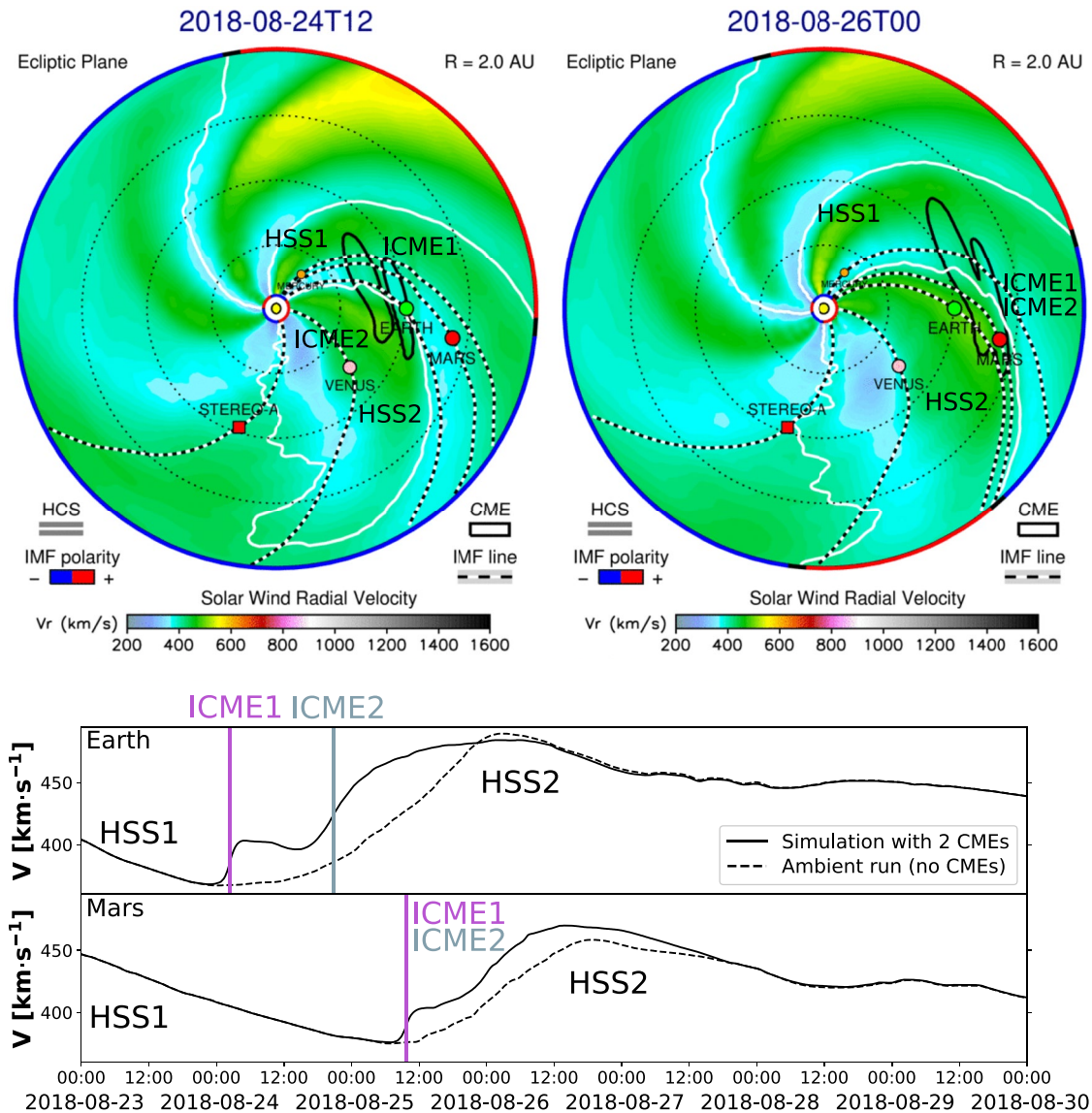


Figure 4. Overview of the WSA–Enlil simulation results at Earth and Mars. Top: Snapshots of the simulation results for the radial speed V_r on the ecliptic plane around the arrival times at (left) Earth and (right) Mars. Bottom: Results for the solar wind speed V at Earth and Mars.

COR2-A field of view (at the times shown in the rightmost column of Figure 2). Both CMEs are inserted with an elliptical cross-section, and their semi-major (ψ_1) and semi-minor (ψ_2) angular extents are obtained by “cutting a slice” out of the GCS shell (see Thernisien, 2011, for details). Finally, the CME insertion speeds (V_0) are calculated from the CME apex height at the time of the last GCS reconstruction (again, shown in the rightmost column of Figure 2) and the height obtained at the reconstruction performed 1 hour earlier, and the insertion times (t_0) are estimated by propagating the “final” CME apex until $21.5 R_\odot$ assuming constant speed V_0 .

An overview of the WSA–Enlil simulation results is shown in Figure 4 and a full animation is shown in Movie S5 in Supporting Information S1. The top panels show snapshots of the solar wind radial speed (V_r) on the ecliptic plane, from which it is evident that both CME1 and CME2 are “sandwiched” between two fast streams marked as “HSS1” and “HSS2”, which we attribute to CH1 and CH2, respectively (see Section 2.1 and Figure 1). “ICME1” and “ICME2” refer to the interplanetary CMEs (ICMEs; e.g., Kilpua et al., 2017) counterparts of CME1 and CME2, respectively. Note that here we refer to ICME as the interplanetary structure as a whole, often composed of a shock, a sheath, and an ejecta. Hence, the ICME arrival time considered here corresponds to the interplanetary shock arrival. By complementing the overall simulation results on the ecliptic plane with the synthetic solar

wind speed (V) measurements at Earth and Mars shown in the bottom panels of Figure 4, it is clear that ICME1 and ICME2 would be expected to impact Earth as successive, largely separate structures, whilst the two would have merged by the time they reach Mars. In the context of the events considered here, there are two possible reasons as to why the slower CME2 would catch up with the initially faster CME1: (a) Due to solar wind preconditioning, resulting in a rarefied ambient medium after the passage of CME1 and, thus, diminished drag (e.g., Temmer & Nitta, 2015), as well as (b) due to the presence of HSS2 trailing CME2, resulting in less deceleration or even acceleration (e.g., Winslow et al., 2021). We approximately estimate ICME1 to hit Earth on 2018-08-24T02:25, ICME2 to hit Earth on 2018-08-24T20:45, and the combined ICME1 + ICME2 structure to hit Mars on 2018-08-25T09:45.

These evaluations and estimates will be used as support to interpret the in-situ measurements at both Earth and Mars, presented in Section 4. Nevertheless, there are a couple of caveats to consider when analyzing these results. For example, the lack of an internal magnetic field in the modeled CMEs inevitably results in unrealistic CME–CME interaction outcomes, since the resulting structure simply corresponds to the superposition of two hydrodynamic pulses. In fact, the ICME ejecta boundaries identified in the simulation (black contours in Figure 4) are estimated in the model via the so-called “cloud tracer” parameter, which tracks the injected mass based on the density enhancement with respect to the background solar wind, that is, they can be considered merely an approximation of the spatial extent of a fully-magnetized ejecta.

4. In-Situ Observations

In this section, we show and analyze in-situ observations following the solar events described in Section 2 at both Earth (Section 4.1) and Mars (Section 4.2). Then, in Section 5, these measurements will be synthesized and discussed in relation to the heliospheric context presented in Section 3.

4.1. Measurements at Earth

In-situ measurements at Earth are shown in Figure 5. They include: magnetic field data from the Magnetic Field Investigation (MFI; Lepping et al., 1995), plasma data from the Solar Wind Experiment (SWE; Ogilvie et al., 1995), and electron pitch angle distribution (PAD) data from the Three-Dimensional Plasma and Energetic Particle Investigation (3DP; Lin et al., 1995) instruments onboard the Wind (Ogilvie & Desch, 1997) spacecraft at the Sun–Earth L1 point; suprathermal and energetic ion data from the Electron, Proton, and Alpha Monitor (EPAM; Gold et al., 1998) onboard the Advanced Composition Explorer (ACE; Stone et al., 1998) also at the Sun–Earth L1 point; space-based galactic cosmic ray (GCR) estimates from the Cosmic Ray Telescope for the Effects of Radiation (CRaTER; Spence et al., 2010) onboard the Lunar Reconnaissance Orbiter (LRO; Chin et al., 2007) orbiting Luna; ground-based GCR estimates from the Thule, Nain, and South Pole stations part of the Neutron Monitor Database (NMDB; Mavromichalaki et al., 2011); as well as Kp index from the National Geophysical Data Center (NGDC) and Dst index from the World Data Center (WDC) for Geomagnetism, Kyoto.

The sequence of events observed at Earth commenced with a weak (i.e., characterized by small downstream-to-upstream ratios in speed, magnetic field magnitude, and plasma density) interplanetary shock (solid pink line in Figure 5) followed by a weak flux-rope-like ejecta (shaded pink region in Figure 5), which we attribute to ICME1, that is, the interplanetary counterpart of CME1. We fit the ejecta with the Elliptic-Cylindrical (EC; Nieves-Chinchilla et al., 2018) analytical flux rope model (shown in blue superposed on the Wind/MFI data in Figure 5), resulting in a moderately inclined structure with axis orientation $(\Theta, \Phi) = (36^\circ, 230^\circ)$ in Geocentric Solar Ecliptic (GSE) coordinates and right-handed chirality, which roughly corresponds to a SWN-type flux rope. About two-thirds into the ICME1 flux rope, a second weak interplanetary shock (solid gray line in Figure 5) was detected, displaying classic shock-in-ejecta signatures (e.g., Lugaz et al., 2015): Proton temperature and plasma beta maintained lower-than-ambient values (typical ICME ejecta indicators; e.g., Zurbuchen & Richardson, 2006) and all the magnetic field components did not display changes in the clock angle after the shock passage. We attribute this shock to ICME2, that is, the interplanetary counterpart of CME2, suggesting that the two eruptions were at the initial stages of their CME–CME interaction process at the time they traveled past Earth. We note no significant particle enhancements in ACE/EPAM data, no Forbush decreases (e.g., Forbush, 1937) in the GCR intensity, and no major geomagnetic effects associated with ICME1 in terms of the Kp and Dst indices. Nevertheless, although the relatively low values of speed, dynamic pressure, and magnetic field did not result in

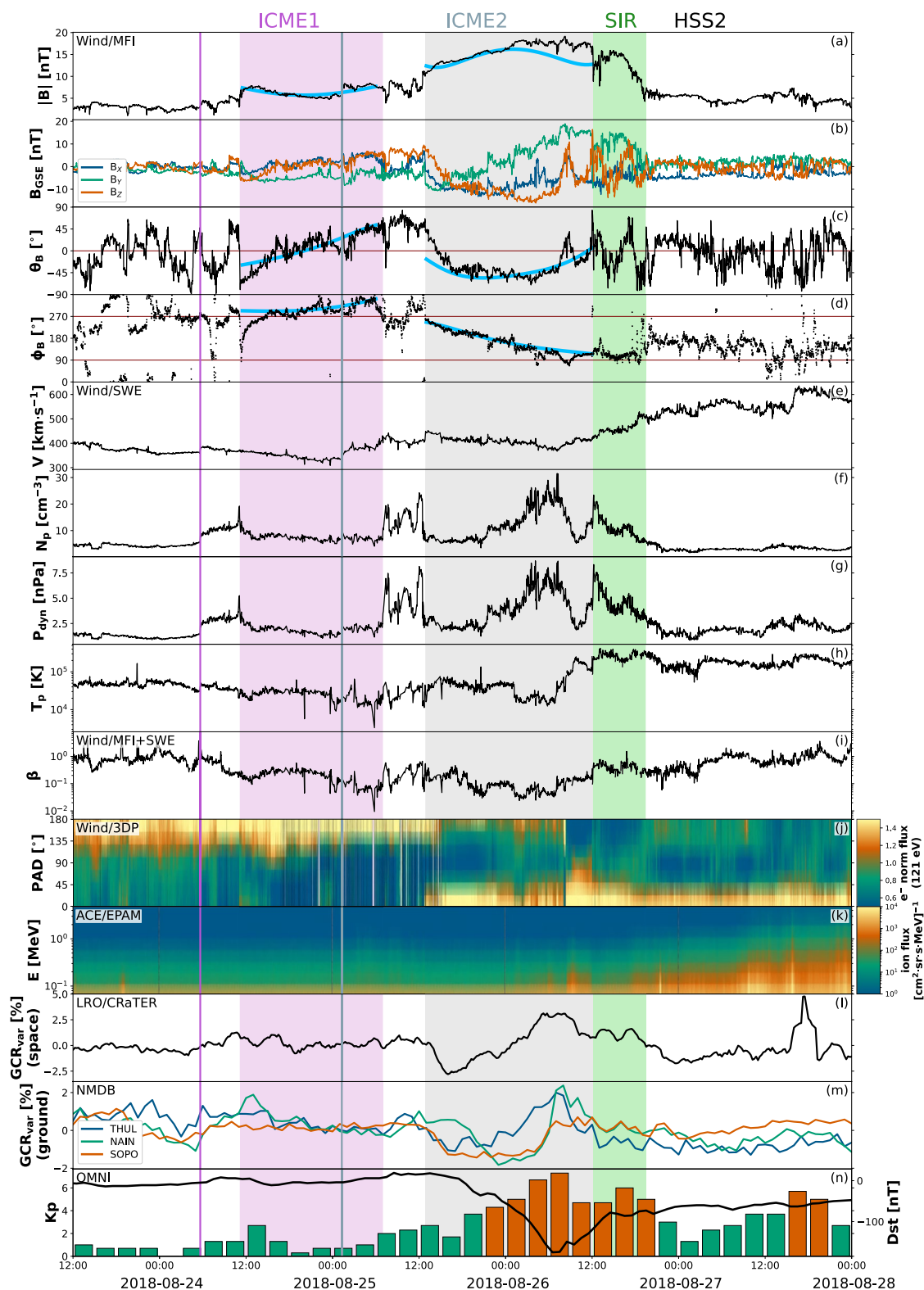


Figure 5. In-situ measurements at Earth, showing (a) magnetic field magnitude, (b) magnetic field components in Geocentric Solar Ecliptic coordinates, (c) θ and (d) ϕ components of the magnetic field, solar wind (e) speed, (f) density, (g) dynamic pressure, and (h) temperature, (i) plasma β , (j) electron pitch angle distribution, (k) ion intensities, galactic cosmic ray variation (l) in space and (m) on ground, and (n) Kp and Dst indices, quantifying geoeffectiveness. The ejecta intervals show flux rope fitting results with the Elliptic-Cylindrical model superposed on the magnetic field data.

a geomagnetic storm, some substorm activity was observed, with the AE index peaking at $\gtrsim 700$ nT (not shown), likely in response to the period of weakly negative B_z in the leading portion of the ICME ejecta.

After a brief period of high density and dynamic pressure measured by Wind/SWE as well as a rather weak but turbulent magnetic field measured by Wind/MFI, which has been interpreted as a signature of interaction between two successive CMEs (Lugaz et al., 2005, 2017; Wang et al., 2003) and evidently part of the ICME2 sheath, a clear flux-rope ejecta (shaded gray region in Figure 5) was detected. Fitting results with the EC model (shown in blue below the Wind/MFI data in Figure 5) yield a left-handed flux rope with a rather high inclination and central axis orientation $(\Theta, \Phi) = (-70^\circ, 145^\circ)$ in GSE coordinates, corresponding roughly to a WSE-type rope. Contrary to ICME1, ICME2 featured clear counterstreaming electron signature in Wind/3DP data and was accompanied by a weak ($\sim 2\%$ drop) Forbush decrease detected both in space by LRO and on ground by different neutron monitors, albeit with slightly different profiles—the LRO/CRAaTER data are closest to the profile measured on ground at the Thule station. Most strikingly, ICME2 was particularly geoeffective, with a maximum K_p of 7+ (corresponding to a G3 storm, see <https://www.swpc.noaa.gov/noaa-scales-explanation>) and a minimum Dst of -175 nT (well exceeding the usual threshold for “strong” storms of $Dst_{\min} \leq -100$ nT; e.g., Zhang et al., 2007), while the AE index peaked at $\gtrsim 2,200$ nT (not shown). These factors make ICME2 the driver of a so-called “problem geomagnetic storm” (Nitta et al., 2021), not because its source was stealthy or elusive (see Nitta & Mulligan, 2017, for a discussion on CMEs without appreciable low-coronal signatures on the Sun), but because its effects at Earth were largely unexpected given the slow and “unimpressive” nature of CME2 at the Sun. In fact, the solar wind speed remained around values of ~ 400 km s $^{-1}$ throughout the ICME passage, indicating that the storm was mostly driven by the sustained southward B_z magnetic field component within the ejecta, which peaked at -16 nT. Other factors contributing to the intensification of the geomagnetic storm may have been the interaction with the preceding ICME1, leading to compression at the front of the ejecta, as well as the presence of a nearby CH (in this case CH2, see Figure 1) back at the Sun, resulting in CME–HSS interaction in interplanetary space and compression in the trailing part of the ejecta (e.g., Nitta et al., 2021).

Indeed, the ICME2 ejecta was immediately followed by a small SIR (shaded green region in Figure 5) and related HSS, most likely due to CH2 and thus indicated in Figure 5 as HSS2. That ICME2 and HSS2 were in the process of interacting is evident by the increasing solar wind speed and temperature detected by Wind/SWE, as well as the particle enhancement at suprathermal energies measured by ACE/EPAM in the trailing part of the ejecta. By the time Earth was impacted by HSS2, the intense geomagnetic storm had essentially waned, with the K_p index briefly reaching again values up to 6—almost a full day later. Nevertheless, a sequence of substorms persisted through the passage of the SIR and the initial portion of the following HSS2, with the AE index peaking between $\sim 1,000$ and $\sim 1,500$ nT for each event (not shown).

4.2. Measurements at Mars

In-situ measurements at Mars are shown in Figure 6. They include: magnetic field data from the Magnetometer (MAG; Connerney et al., 2015), plasma data from the Solar Wind Ion Analyzer (SWIA; Halekas et al., 2015), electron PAD data from the Solar Wind Electron Analyzer (SWEA; Mitchell et al., 2016), and suprathermal/energetic ion data as well as space-based GCR estimates from the Solar Energetic Particle (SEP; Larson et al., 2015) instruments onboard the Mars Atmosphere and Volatile Evolution (MAVEN; Jakosky, Lin, et al., 2015) spacecraft orbiting Mars; plasma data from the Analyzer of Space Plasmas and Energetic Atoms (ASPERA-3; Barabash et al., 2006) onboard Mars Express (MEX; Chicarro et al., 2004) also orbiting Mars; ground-based GCR estimates from the Radiation Assessment Detector (RAD; Hassler et al., 2012) onboard the Curiosity rover part of the Mars Science Laboratory (MSL; Grotzinger et al., 2012); and Magnetospheric Disturbance Index (MDI; Gruesbeck et al., 2021) data. MDI takes MAVEN/MAG measurements as input and is used to estimate the level of the disturbance to the Martian system, or arieffectiveness.

The sequence of events at Mars commenced again with a possible weak interplanetary shock (solid pink line in Figure 6), identified mainly via a peak in ion fluxes at suprathermal energies detected by MAVEN/SEP because of the frequent gaps in magnetic field and plasma data. In fact, these data gaps are due to the MAVEN and MEX orbits, resulting in only a portion of their path around Mars sampling the upstream solar wind. The MEX/ASPERA-3 measurements displayed in Figure 6 consist of averages along the spacecraft's orbit, and the MAVEN/MAG and MAVEN/SWIA data show solar wind periods identified according to the algorithm of Halekas et al. (2017). The MAVEN/MAG measurements shown in lighter colors represent data that are not

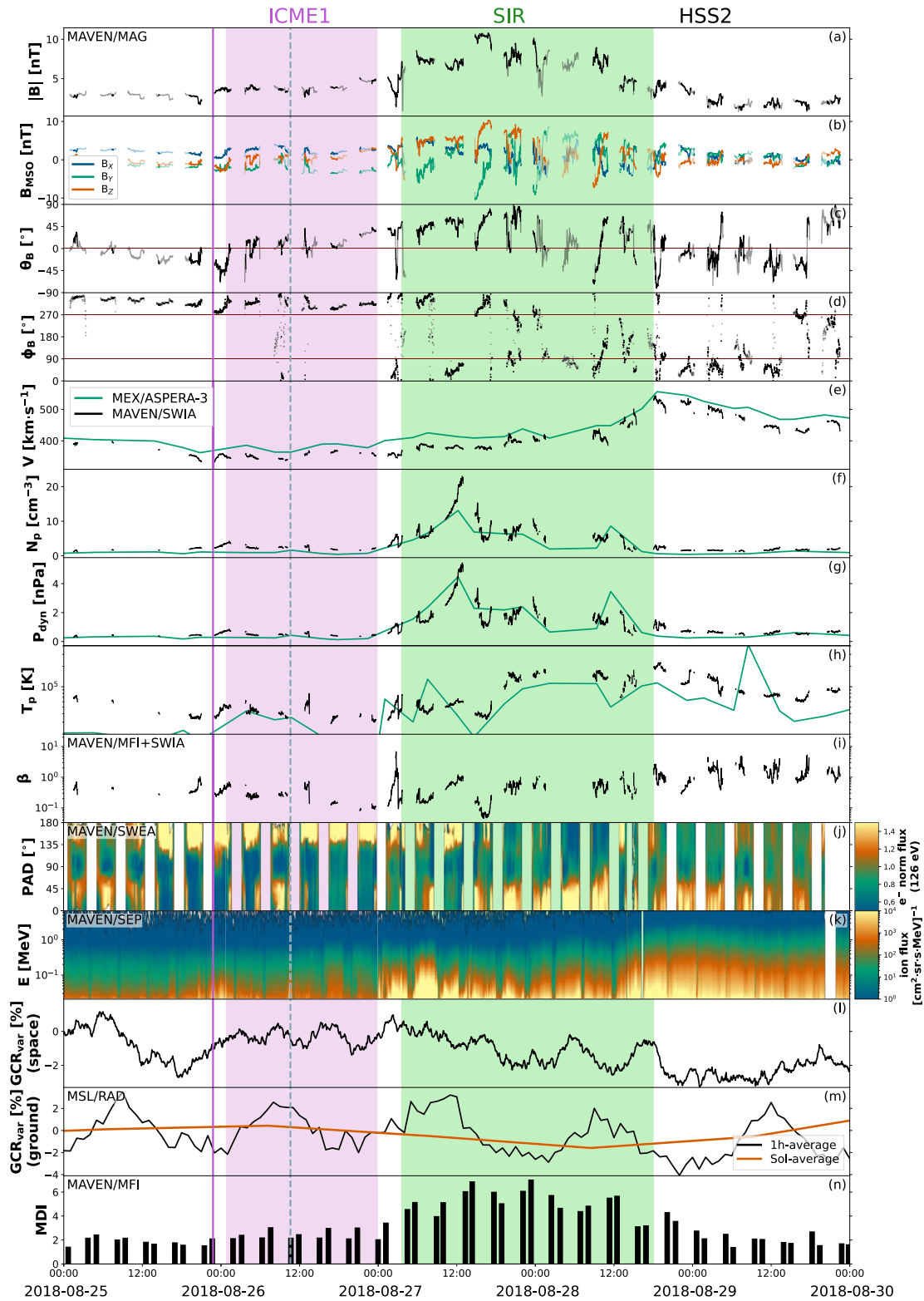


Figure 6. In-situ measurements at Mars, showing (a) magnetic field magnitude, (b) magnetic field components in Mars Solar Orbital coordinates, (c) θ and (d) ϕ components of the magnetic field, solar wind (e) speed, (f) density, (g) dynamic pressure, and (h) temperature, (i) plasma β , (j) electron pitch angle distribution, (k) ion intensities, galactic cosmic ray variation (l) in space and (m) on ground, and (n) Magnetospheric Disturbance Index index, quantifying arieeffectiveness. The lighter portions of magnetic field data are sampled in the Martian foreshock rather than in the solar wind.

part of the “undisturbed” solar wind but are still outside the Martian bow shock, that is, they are collected in the foreshock region. The possible interplanetary shock is followed by a weak ejecta (shaded pink region in Figure 6), with directions of the magnetic field vectors closely resembling those observed at Earth for ICME1 (see Figure 5). The θ_B component rotates from south to north and the ϕ_B one points to the west in Mars Solar Orbital (MSO) coordinates (i.e., the GSE equivalent for Mars), indicating a SWN-type flux rope. Considering the ICME1 shock speed at Earth ($\sim 385 \text{ km s}^{-1}$) and the Earth–Mars radial distance at the time of $\sim 0.4 \text{ AU}$, the structure would have taken $\sim 43 \text{ hr}$ to propagate from one planet to the next, in agreement with the timing of the observed candidate shock at Mars. Hence, we attribute this structure to ICME1. Approximately in the middle of the ejecta, we identify a possible second interplanetary shock (dashed gray line in Figure 6), again because of a small enhancement in the MAVEN/SEP spectrum and because the solar wind speed measured by MAVEN/SWIA displays a small increase afterward. This is likely the ICME2 shock, still traveling through the ICME1 ejecta—again, the timing ($\sim 44 \text{ hr}$ for a shock moving at $\sim 380 \text{ km s}^{-1}$ across $\sim 0.4 \text{ AU}$) is consistent between the observations at Earth and Mars. ICME1 was characterized by some periods of bidirectional electrons measured by MAVEN/SWEA, especially during the first half of the ejecta, no Forbush decreases in space nor on ground, and no significant disturbances to the Martian system.

After the passage of the weak ICME1, a period of clear enhanced magnetic field magnitude followed (shaded green region in Figure 6). However, this structure displays classic signatures of a SIR rather than of an ICME (e.g., Kataoka & Miyoshi, 2006), including the absence of an organized internal magnetic field throughout its extent, and an increase in solar wind speed and temperature as well as a decrease in density at the stream interface. This suggests that the ejecta of ICME2, which was rather prominent at Earth (see Figure 5), largely missed Mars. It is unclear whether minor portions of the ejecta interacted and/or merged with the following SIR at Mars’s heliolongitude, especially given the numerous data gaps throughout the structure. The plasma profiles measured by MAVEN/SWIA in the first half of the SIR resemble those observed at Earth in the ICME2 ejecta and following SIR (see Figure 5), but the absence of bidirectional electrons in MAVEN/SWEA data as well as the disorganized magnetic field components seen by MAVEN/MAG suggest that, if material from CME2 was indeed detected at Mars, the ejecta had lost its coherence and flux rope structure (at least locally) due to interaction with the structured solar wind. The SIR was accompanied by enhanced ion fluxes measured by MAVEN/SEP at sub-MeV energies (see Richardson, 2004, for a review on SIR-associated energetic particle observations), as well as by a weak ($\sim 2\%$ drop) Forbush decrease measured both in space by MAVEN/SEP and on ground by MSL/RAD (see Guo et al., 2018, for an overview of space- and ground-based observations of CME- and SIR-driven Forbush decreases at Mars). We note that no significant variations were detected in the MEX/ASPERA-3 Ion Mass Analyzer (IMA) background counts (not shown), which can be used as proxies for GCR intensity (see Futaana et al., 2022, for a description of the data set). Additionally, the SIR was rather ineffective according to MDI values, peaking at ~ 7 —we note that Gruesbeck et al. (2021) reported a peak MDI of ~ 4 for the 8 March 2015 ICME studied by Jakosky, Grebowsky, et al. (2015) and of ~ 10 for the 13 September 2017 ICME analyzed by Lee et al. (2018). Finally, as expected, the SIR was ultimately followed by HSS2.

5. Discussion

The eruptive events that took place during the second half of August 2018 were typical of solar minimum conditions: They did not originate from active regions nor did they display an “explosive” nature, they were slow, and they were rather “isolated” (i.e., there was no other activity elsewhere on the Sun during the same period). Nevertheless, such a seemingly simple picture resulted in a number of unexpected outcomes, including a major problem storm at Earth and a missed CME impact at Mars, despite the small ($<10^\circ$) longitudinal separation between the two planets. Here, we synthesize the solar and heliospheric observations discussed in the previous sections together with the WSA–Enlil modeling results, and elaborate on the possible evolutionary scenario that is consistent with measurements at both planets.

First of all, we note that the CME arrival times estimated by WSA–Enlil (see Figure 4) are between $\sim 4 \text{ hr}$ (ICME1 at Earth) to $\sim 12 \text{ hr}$ (ICME1 at Mars) too early compared to observations. This is likely due to HSS2 impacting Earth approximately 1 day too early and Mars approximately 2 days too early in the simulation, resulting in a diminished deceleration of the CMEs ahead due to solar wind drag. Nevertheless, Gressl et al. (2014) found that predicted HSS arrival times in MHD models have uncertainties of the order of about 1 day, suggesting that the period under analysis was not particularly challenging in terms of characterizing the solar wind background,

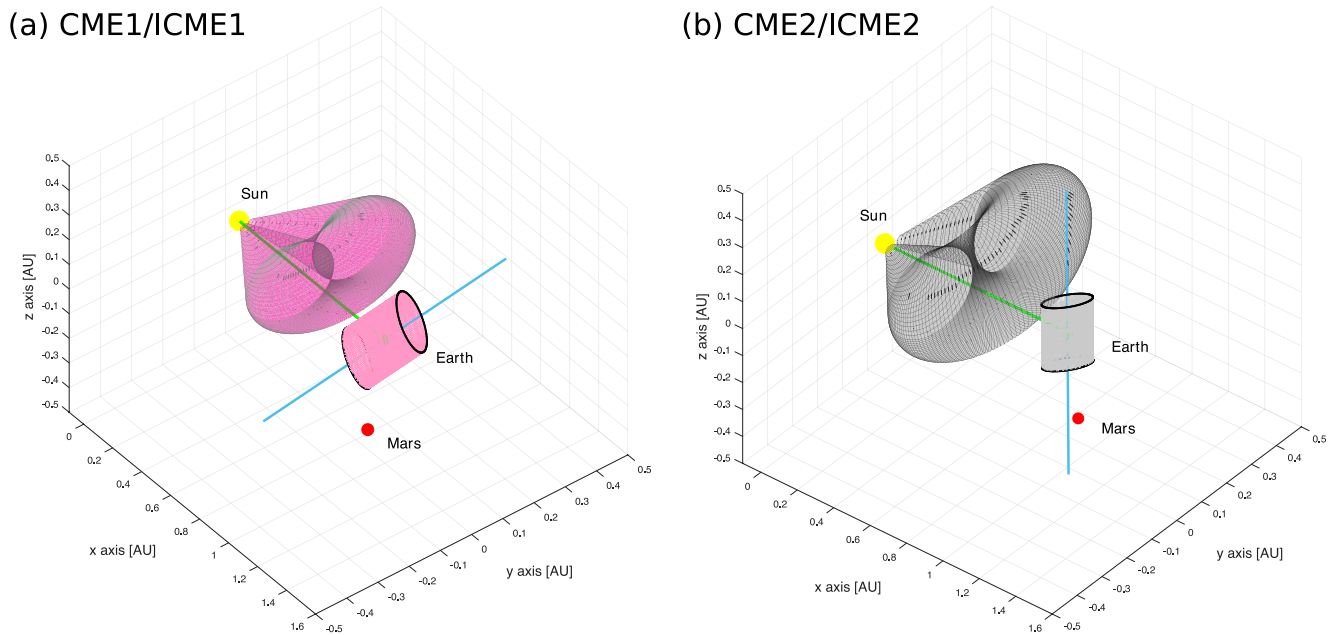


Figure 7. Comparison of the Graduated Cylindrical Shell (GCS)-derived coronal mass ejection (CME) orientation in the solar corona and Elliptic-Cylindrical (EC)-derived interplanetary coronal mass ejection (ICME) ejecta orientation at Earth for (a) CME1/ICME1, in pink, and (b) CME2/ICME2, in gray. The crossant-like features show the CME morphology obtained via the GCS reconstructions shown in Figure 2, whilst the cylinders represent the corresponding ICME structures retrieved via the EC fits displayed in Figure 5.

since it was affected by typical errors. Arrival times aside, the sequence of events at Earth was well reproduced in the simulation (see Movie S5 in Supporting Information S1 for a more complete view of the modeling results): ICME2 closely followed ICME1 (and the eruptions had just started to interact by the time they crossed Earth) and was immediately trailed by HSS2. What was impossible to forecast from the WSA–Enlil simulation was the impressive magnitude of the geomagnetic storm driven by ICME2.

In fact, the factors that led to the unexpected geoeffectiveness of ICME2 at Earth may also explain why the same structure missed Mars. This is illustrated in Figure 7, which shows a comparison of the CME flux rope orientations retrieved from solar observations (i.e., the GCS reconstructions in Figure 2) and in-situ measurements at Earth (i.e., the EC fits in Figure 5). It is evident that CME1/ICME1 maintained a low inclination to the equatorial plane throughout its heliospheric evolution, resulting in a flux rope type that was estimated to be SWN in the solar corona, at Earth, and later at Mars. CME2, on the other hand, left the Sun with a WSE configuration but was later observed in the solar corona to have assumed a lowly-inclined orientation (possibly NWS, see especially its morphology in SOHO/LASCO data in Figures 2m–2p). At Earth, however, the retrieved flux rope type of ICME2 was again WSE, leading to the strong southward field that mainly drove the observed geomagnetic storm. We speculate that interaction with the following HSS2 resulted in both CME rotation toward a high-inclination configuration and CME deflection toward western heliolongitudes. The latter effect is marginally visible in the WSA–Enlil simulation (see Movie S5 in Supporting Information S1), whilst the former could not be reproduced with the current set up since the two CMEs have been modeled without an internal magnetic field, leading to unrealistic CME–CME and CME–HSS interaction processes. The rotation and deflection of the CME2 flux rope ejecta in interplanetary space may account for the fact that only the ICME2 shock seems to have impacted Mars. Of course, these considerations imply that CME2 was indeed characterized by a low inclination with respect to the solar equator throughout the solar corona—since the GCS reconstructions were performed using the only two available viewpoints of Earth (halo event) and STEREO-A (limb event), the resulting morphology may have been under-constrained and thus associated with rather large uncertainties.

Another interesting result is that, whilst Mars was not impacted by the ICME2 ejecta, it was still affected by significant large-scale disturbances during the period under study, namely due to the SIR ahead of HSS2. At Earth, the SIR was not particularly geoeffective, suggested by the fact that the Dst index did not display a second dip after the passage of ICME2 (although it does appear to have interrupted the recovery of the ongoing storm)—

it is worth noting, however, that the presence of ICME2 at Earth likely impeded the formation of a proper slow-fast SIR, and that what we identified as a small SIR displays characteristics of a CME–HSS interaction region. At Mars, the SIR passage lasted for over a day and was fundamentally responsible for the observed arieeffectiveness. We remark, nevertheless, that the plasma signatures in the first half of the SIR at Mars displayed similarities with those observed in the ICME2 ejecta at Earth, possibly indicating that some material from CME2 may have become part of the SIR due to interaction with the structured solar wind. Whilst it is not known whether similar effects would have been experienced at Mars had the ICME2 ejecta impacted the planet as a well-defined flux rope structure, we can speculate that, during solar minimum conditions, when CMEs are on average less energetic, we may generally expect higher arieeffectiveness from SIRs than from ICMEs (contrarily to Earth, where the most geoeffective structures are associated with CMEs across the whole solar cycle; e.g., Richardson et al., 2001). In fact, whilst CMEs tend to expand (and thus experience a decrease in speed, density, and dynamic pressure) until ~ 10 – 15 AU, where they reach pressure balance with the ambient wind (e.g., von Steiger and Richardson, 2006), SIRs are known to increase the compression of the fast stream against the slow stream with heliocentric distance until a few AUs (e.g., Forsyth & Marsch, 1999)—for example, Jian et al. (2008) found a significant increase in SIR-associated shock detections from Venus to Earth, and Geyer et al. (2021) found that the occurrence of SIR-driven fast-forward shocks is three times higher at Mars than at Earth. Additionally, Edberg et al. (2010) found that most solar wind pressure pulse events—which lead to a 2.5-fold increase in atmospheric escape—correspond to SIR drivers, whilst only a few are driven by CMEs.

6. Concluding Remarks

In this work, we have analyzed the eruption, evolution, and impact at Earth and Mars of a series of solar transients during the second half of August 2018, that is, close to the activity minimum between solar cycles 24–25. In particular, we have tracked the eruption (on 20 August 2018) and propagation of two CMEs (CME1 and CME2) throughout their journey in the inner heliosphere as they were followed by a fast solar wind stream (HSS2). We found that both planets experienced space weather effects, but due to different drivers: at Earth, an ICME ejecta (ICME2) with a strong southward component of its magnetic field was the main driver of a major geomagnetic storm, whilst at Mars, the main structure responsible for the observed arieeffectiveness was a SIR. The first event in the sequence of transients, that is, a preceding, smaller ICME (ICME1), was detected at both planets but had no significant effects on their space environments.

We also compared in-situ measurements at Earth and Mars with simulation results using the MHD WSA–Enlil model. First of all, we noted that the observed geomagnetic storm could not have been predicted with the used set up, since the CMEs were modeled without an internal magnetic field. Heliospheric models that include a magnetized CME are expected to provide more realistic insights into the dynamics of CME–CME and CME–HSS interaction (e.g., Asvestari et al., 2022; Scolini et al., 2020). The hydrodynamic nature of the modeled CMEs may also explain why CME2 was predicted to merge with CME1 beyond 1 AU and ultimately impact Mars, whilst it likely rotated and drifted toward western heliolongitudes due to interactions with the following HSS2.

At Mars, the SIR-induced effects would have been predicted more successfully with the modeling set up used in this study, although the HSS of interest (HSS2) was simulated to arrive earlier than observed at both planets. Riley et al. (2012) found that global MHD models can diverge more or less significantly from observations in capturing the overall structure of the ambient solar wind even for solar minimum periods, when conditions are relatively steady. Jian et al. (2011) reported that SIR timing predictions can have temporal offsets of up to 2 days at 1 AU and up to 4 days at 5 AU. Large-scale efforts dedicated to benchmarking solar wind models (e.g., Reiss et al., 2022) will likely lead to improved predictions of solar wind structures (including SIRs and CMEs) and their effects at different planets. In fact, a well-constrained and well-reproduced solar wind background is of great importance for simulating solar minimum CMEs, which tend to alter their structure and orientation during propagation largely due to interactions with the steady wind (see, e.g., the May 1997 event; Cohen et al., 2010; Odstroil et al., 2004; Titov et al., 2008).

Finally, we comment on two aspects that may be of interest to martian space weather research. First, although most major geomagnetic storm are associated with CMEs, it has been reported that SIRs can occasionally drive strong responses at Earth (Richardson et al., 2006). Given that SIRs are expected to strengthen beyond 1 AU, an interesting exercise would be to follow one such strongly geoeffective structure from Earth to Mars and evaluate its arieeffectiveness—as space weather at Mars is a relatively novel area of research, it is currently unclear which

solar wind transients are generally associated with the most severe disturbances. Additionally, the different types of magnetospheres may lead to different solar wind driving conditions at Earth and Mars. Of course, analysis of the solar wind drivers of martian storms would strongly benefit from continuous space weather monitoring, perhaps via a satellite placed at the Sun–Mars L1 point as is the case for Earth (e.g., Sánchez-Cano et al., 2021).

Data Availability Statement

Solar disc and coronagraph data from SDO, SOHO, and STEREO are openly available at the Virtual Solar Observatory (VSO; <https://sdac.virtualsolar.org/>), whilst STEREO/HI Level-2 data can be retrieved from the UK Solar System Data Center (UKSSDC; <https://www.ukssdc.ac.uk>). These data were visualized, processed, and analyzed through SunPy (The SunPy Community et al., 2020), IDL SolarSoft (Bentley & Freeland, 1998), and the ESA JHelioviewer software (Müller et al., 2017). Enlil simulation results have been provided by the Community Coordinated Modeling Center at Goddard Space Flight Center through their public Runs on Request system (<http://ccmc.gsfc.nasa.gov>). The full simulation results are available at https://ccmc.gsfc.nasa.gov/results/viewrun.php?domain=SH&runnumber=Erika_Palmerio_050922_SH_1 (run id: Erika_Palmerio_050922_SH_1). Wind and ACE data are publicly available at NASA's Coordinated Data Analysis Web (CDAWeb) database (<https://cdaweb.gsfc.nasa.gov/index.html>). NMDB data are publicly available at <http://www.nmdb.eu>. LRO, MAVEN, and MSL data can be accessed at the Planetary Plasma Interactions (PPI) Node of NASA's Planetary Data System (PDS) database (<https://pds-ppi.igpp.ucla.edu>). MEX data are openly available at ESA's Planetary Science Archive (PSA) database (<https://archives.esac.esa.int/psa>).

Acknowledgments

E. Palmerio acknowledges the NASA Living With a Star (LWS) Jack Eddy Postdoctoral Fellowship Program, administered by UCAR's Cooperative Programs for the Advancement of Earth System Science (CPAESS) under award no. NNX16AK22G, as well as NASA's HTMS Program (no. 80NSSC20K1274) and NSF's PREEVENTS Program (no. ICER-1854790). C. O. Lee, J. R. Gruesbeck, J. S. Halekas, and S. Xu acknowledge support from the MAVEN mission, which is supported by NASA through the Mars Exploration Program. C. O. Lee, S. Xu, B. J. Lynch, and J. G. Luhmann acknowledge NASA HGI (no. 80NSSC21K0731) and LWS (no. 80NSSC21K1325). I. G. Richardson acknowledges support from NASA LWS Program NNH19ZDA001N-LWS. The WSA model was developed by C. N. Arge (currently at NASA/GSFC), and the Enlil model was developed by D. Odstrcil (currently at GMU). We thank the model developers and the CCMC staff. E. Palmerio, I. G. Richardson, N. V. Nitta, T. Mulligan, and B. J. Lynch thank the International Space Science Institute (ISSI) for their support of International Team no. 415, "Understanding the Origins of Problem Geomagnetic Storms" (<https://www.issibern.ch/teams/geomagstorm/>).

References

- Abunin, A. A., Abunina, M. A., Belov, A. V., & Chertok, I. M. (2020). Peculiar solar sources and geospace disturbances on 20–26 August 2018. *Solar Physics*, 295(1), 7. <https://doi.org/10.1007/s11207-019-1574-8>
- Acuna, M. H., Connerney, J. E. P., Wasilewski, P., Lin, R. P., Anderson, K. A., Carlson, C. W., et al. (1998). Magnetic field and plasma observations at Mars: Initial results of the Mars global surveyor mission. *Science*, 279(5357), 1676–1680. <https://doi.org/10.1126/science.279.5357.1676>
- Akala, A. O., Oyedokun, O. J., Amaechi, P. O., Simi, K. G., Ogwala, A., & Arowolo, O. A. (2021). Solar origins of August 26, 2018 geomagnetic storm: Responses of the interplanetary medium and equatorial/low-latitude ionosphere to the storm. *Space Weather*, 19(10), e2021SW002734. <https://doi.org/10.1029/2021SW002734>
- Arge, C. N., Luhmann, J. G., Odstrcil, D., Schrijver, C. J., & Li, Y. (2004). Stream structure and coronal sources of the solar wind during the May 12th, 1997 CME. *Journal of Atmospheric and Solar-Terrestrial Physics*, 66(15–16), 1295–1309. <https://doi.org/10.1016/j.jastp.2004.03.018>
- Asvestari, E., Rindlisbacher, T., Pomoell, J., & Kilpua, E. K. J. (2022). The spheromak tilting and how it affects modeling coronal mass ejections. *The Astrophysical Journal*, 926(1), 87. <https://doi.org/10.3847/1538-4357/ac3a73>
- Barabash, S., Lundin, R., Andersson, H., Brinkfeldt, K., Grigoriev, A., Gunell, H., et al. (2006). The analyzer of space plasmas and energetic atoms (ASPERA-3) for the Mars Express mission. *Space Science Reviews*, 126(1–4), 113–164. <https://doi.org/10.1007/s11214-006-9124-8>
- Bentley, R. D., & Freeland, S. L. (1998). SOLARSOFT—An analysis environment for solar physics. In *Crossroads for European solar and heliospheric physics. Recent achievements and future mission possibilities* (Vol. 417, p. 225). ESA Special Publication.
- Benz, A. O. (2017). Flare observations. *Living Reviews in Solar Physics*, 14(1), 2. <https://doi.org/10.1007/s41116-016-0004-3>
- Bertucci, C., Duru, F., Edberg, N., Fraenz, M., Martinecz, C., Szego, K., & Vaisberg, O. (2011). The induced magnetospheres of Mars, Venus, and Titan. *Space Science Reviews*, 162(1–4), 113–171. <https://doi.org/10.1007/s11214-011-9845-1>
- Bothmer, V., & Schwenn, R. (1998). The structure and origin of magnetic clouds in the solar wind. *Annales Geophysicae*, 16, 1–24. <https://doi.org/10.1007/s00585-997-0001-x>
- Brueckner, G. E., Howard, R. A., Koomen, M. J., Korendyke, C. M., Michels, D. J., Moses, J. D., et al. (1995). The large angle spectroscopic coronagraph (LASCO). *Solar Physics*, 162(1–2), 357–402. <https://doi.org/10.1007/BF00733434>
- Chen, C., Liu, Y. D., Wang, R., Zhao, X., Hu, H., & Zhu, B. (2019). Characteristics of a gradual filament eruption and subsequent CME propagation in relation to a strong geomagnetic storm. *The Astrophysical Journal*, 884(1), 90. <https://doi.org/10.3847/1538-4357/ab3f36>
- Cherniak, I., & Zakharenkova, I. (2022). Development of the storm-induced ionospheric irregularities at equatorial and middle latitudes during the 25–26 August 2018 geomagnetic storm. *Space Weather*, 20(2), e2021SW002891. <https://doi.org/10.1029/2021SW002891>
- Chicarro, A., Martin, P., & Trautner, R. (2004). The Mars express mission: An overview. In A. Wilson & A. Chicarro (Eds.), *Mars express: The scientific payload* (Vol. 1240, pp. 3–13). ESA Special Publication.
- Chin, G., Brylow, S., Foote, M., Garvin, J., Kasper, J., Keller, J., et al. (2007). Lunar reconnaissance orbiter overview: The instrument suite and mission. *Space Science Reviews*, 129(4), 391–419. <https://doi.org/10.1007/s11214-007-9153-y>
- Cohen, O., Attrill, G. D. R., Schwadron, N. A., Crooker, N. U., Owens, M. J., Downs, C., & Gombosi, T. I. (2010). Numerical simulation of the 12 May 1997 CME Event: The role of magnetic reconnection. *Journal of Geophysical Research*, 115(A10), A10104. <https://doi.org/10.1029/2010JA015464>
- Connerney, J. E. P., Espley, J., Lawton, P., Murphy, S., Odom, J., Oliverson, R., & Sheppard, D. (2015). The MAVEN magnetic field investigation. *Space Science Reviews*, 195(1–4), 257–291. <https://doi.org/10.1007/s11214-015-0169-4>
- Crider, D. H., Espley, J., Brain, D. A., Mitchell, D. L., Connerney, J. E. P., & Acuña, M. H. (2005). Mars Global Surveyor observations of the Halloween 2003 solar superstorm's encounter with Mars. *Journal of Geophysical Research*, 110(A9), A09S21. <https://doi.org/10.1029/2004JA010881>
- DiBraccio, G. A., Luhmann, J. G., Curry, S. M., Espley, J. R., Xu, S., Mitchell, D. L., et al. (2018). The Twisted configuration of the martian magnetotail: MAVEN observations. *Geophysical Research Letters*, 45(10), 4559–4568. <https://doi.org/10.1029/2018GL077251>
- Domingo, V., Fleck, B., & Poland, A. I. (1995). The SOHO mission: An overview. *Solar Physics*, 162(1–2), 1–37. <https://doi.org/10.1007/BF00733425>
- Edberg, N. J. T., Nilsson, H., Williams, A. O., Lester, M., Milan, S. E., Cowley, S. W. H., et al. (2010). Pumping out the atmosphere of Mars through solar wind pressure pulses. *Geophysical Research Letters*, 37(3), L03107. <https://doi.org/10.1029/2009GL041814>

- Eyles, C. J., Harrison, R. A., Davis, C. J., Waltham, N. R., Shaughnessy, B. M., Mapson-Menard, H. C. A., et al. (2009). The heliospheric imagers onboard the STEREO mission. *Solar Physics*, *254*(2), 387–445. <https://doi.org/10.1007/s11207-008-9299-0>
- Forbush, S. E. (1937). On the effects in cosmic-ray intensity observed during the recent magnetic storm. *Physical Review*, *51*(12), 1108–1109. <https://doi.org/10.1103/PhysRev.51.1108.3>
- Forsyth, R. J., & Marsch, E. (1999). Solar origin and interplanetary evolution of stream interfaces. *Space Science Reviews*, *89*(1/2), 7–20. <https://doi.org/10.1023/A:1005235626013>
- Futaana, Y., Shimoyama, M., Wieser, M., Karlsson, S., Andersson, H., Nilsson, H., et al. (2022). Galactic Cosmic Rays at Mars and Venus: Temporal Variations from Hours to Decades Measured as the Background Signal of Onboard Micro-Channel Plates, arXiv e-prints, arXiv:2204.01377.
- Galvin, A. B., & Kohl, J. L. (1999). Whole Sun Month at solar minimum: An introduction. *Journal of Geophysical Research*, *104*(A5), 9673–9678. <https://doi.org/10.1029/1999JA900008>
- Geyer, P., Temmer, M., Guo, J., & Heinemann, S. G. (2021). Properties of stream interaction regions at Earth and Mars during the declining phase of SC 24. *Astronomy & Astrophysics*, *649*, A80. <https://doi.org/10.1051/0004-6361/202040162>
- Gold, R. E., Krimigis, S. M., Hawkins, S. E., Haggerty, D. K., Lohr, D. A., Fiore, E., et al. (1998). Electron, Proton, and Alpha monitor on the advanced composition explorer spacecraft. *Space Science Reviews*, *86*(1/4), 541–562. <https://doi.org/10.1023/A:1005088115759>
- Gonzalez, W. D., Joselyn, J. A., Kamide, Y., Kroehl, H. W., Rostoker, G., Tsurutani, B. T., & Vasyliunas, V. M. (1994). What is a geomagnetic storm? *Journal of Geophysical Research*, *99*(A4), 5771–5792. <https://doi.org/10.1029/93JA02867>
- Gopalswamy, N., Yashiro, S., Akiyama, S., Xie, H., Mäkelä, P., Fok, M.-C., & Ferradas, C. P. (2022). What is unusual about the third largest geomagnetic storm of solar cycle 24? *Journal of Geophysical Research: Space Physics*, *127*(8), e2022JA030404. <https://doi.org/10.1029/2022JA030404>
- Green, L. M., Kliem, B., Török, T., van Driel-Gesztelyi, L., & Attrill, G. D. R. (2007). Transient coronal sigmoids and rotating erupting flux ropes. *Solar Physics*, *246*(2), 365–391. <https://doi.org/10.1007/s11207-007-9061-z>
- Gressl, C., Veronig, A. M., Temmer, M., Odstrčil, D., Linker, J. A., Mikić, Z., & Riley, P. (2014). Comparative study of MHD modeling of the background solar wind. *Solar Physics*, *289*(5), 1783–1801. <https://doi.org/10.1007/s11207-013-0421-6>
- Grotzinger, J. P., Crisp, J., Vasavada, A. R., Anderson, R. C., Baker, C. J., Barry, R., et al. (2012). Mars Science Laboratory mission and science investigation. *Space Science Reviews*, *170*(1–4), 5–56. <https://doi.org/10.1007/s11214-012-9892-2>
- Gruesbeck, J. R., Espley, J. R., Lee, C. O., & Curry, S. M. (2021). A generalized magnetospheric disturbance index: Initial application to Mars using MAVEN observations. *Journal of Geophysical Research: Space Physics*, *126*(12), e2021JA029479. <https://doi.org/10.1029/2021JA029479>
- Guo, J., Lillis, R., Wimmer-Schweingruber, R. F., Zeitlin, C., Simonson, P., Rahmati, A., et al. (2018). Measurements of Forbush decreases at Mars: Both by MSL on ground and by MAVEN in orbit. *Astronomy & Astrophysics*, *611*, A79. <https://doi.org/10.1051/0004-6361/201732087>
- Halekas, J. S., Ruhunusiri, S., Harada, Y., Collinson, G., Mitchell, D. L., Mazelle, C., et al. (2017). Structure, dynamics, and seasonal variability of the Mars-solar wind interaction: MAVEN solar wind ion analyzer in-flight performance and science results. *Journal of Geophysical Research: Space Physics*, *122*(1), 547–578. <https://doi.org/10.1002/2016JA023167>
- Halekas, J. S., Taylor, E. R., Dalton, G., Johnson, G., Curtis, D. W., McFadden, J. P., et al. (2015). The solar wind ion analyzer for MAVEN. *Space Science Reviews*, *195*(1–4), 125–151. <https://doi.org/10.1007/s11214-013-0029-z>
- Harvey, J. W., Hill, F., Hubbard, R. P., Kennedy, J. R., Leibacher, J. W., Pintar, J. A., et al. (1996). The global oscillation network group (GONG) project. *Science*, *272*(5266), 1284–1286. <https://doi.org/10.1126/science.272.5266.1284>
- Hassler, D. M., Zeitlin, C., Wimmer-Schweingruber, R. F., Böttcher, S., Martin, C., Andrews, J., et al. (2012). The radiation assessment detector (RAD) investigation. *Space Science Reviews*, *170*(1–4), 503–558. <https://doi.org/10.1007/s11214-012-9913-1>
- Hathaway, D. H. (2015). The solar cycle. *Living Reviews in Solar Physics*, *12*(1), 4. <https://doi.org/10.1007/lrsp-2015-4>
- Howard, R. A., Moses, J. D., Vourlidas, A., Newmark, J. S., Socker, D. G., Plunkett, S. P., et al. (2008). Sun Earth connection coronal and heliospheric investigation (SECCHI). *Space Science Reviews*, *136*(1–4), 67–115. <https://doi.org/10.1007/s11214-008-9341-4>
- Huang, H., Guo, J., Mazelle, C., Penou, E., Lin, H., & Zhao, D. (2021). Properties of interplanetary fast shocks close to the martian environment. *The Astrophysical Journal*, *914*(1), 14. <https://doi.org/10.3847/1538-4357/abf82b>
- Jakosky, B. M., Grebowsky, J. M., Luhmann, J. G., Connerney, J. E., Eparvier, F., Ergun, R., et al. (2015). MAVEN observations of the response of Mars to an interplanetary coronal mass ejection. *Science*, *350*(6261), 0210. <https://doi.org/10.1126/science.aad0210>
- Jakosky, B. M., Lin, R. P., Grebowsky, J. M., Luhmann, J. G., Mitchell, D. F., Beutelschies, G., et al. (2015). The Mars atmosphere and volatile evolution (MAVEN) mission. *Space Science Reviews*, *195*(1–4), 3–48. <https://doi.org/10.1007/s11214-015-0139-x>
- Jian, L., Russell, C. T., Luhmann, J. G., & Skoug, R. M. (2008). Evolution of solar wind structures from 0.72 to 1 AU. *Advances in Space Research*, *41*(2), 259–266. <https://doi.org/10.1016/j.asr.2007.03.023>
- Jian, L. K., Russell, C. T., Luhmann, J. G., MacNeice, P. J., Odstrčil, D., Riley, P., et al. (2011). Comparison of observations at ACE and Ulysses with Enlil model results: Stream interaction regions during Carrington rotations 2016–2018. *Solar Physics*, *273*(1), 179–203. <https://doi.org/10.1007/s11207-011-9858-7>
- Kaiser, M. L., Kucera, T. A., Davila, J. M., Cyr, O. C. S., Guhathakurta, M., & Christian, E. (2008). The STEREO mission: An introduction. *Space Science Reviews*, *136*(1–4), 5–16. <https://doi.org/10.1007/s11214-007-9277-0>
- Kajdič, P., Sánchez-Cano, B., Neves-Ribeiro, L., Witasse, O., Bernal, G. C., Rojas-Castillo, D., et al. (2021). Interaction of space weather phenomena with Mars plasma environment during solar minimum 23/24. *Journal of Geophysical Research: Space Physics*, *126*(2), e2020JA028442. <https://doi.org/10.1029/2020JA028442>
- Kataoka, R., & Miyoshi, Y. (2006). Flux enhancement of radiation belt electrons during geomagnetic storms driven by coronal mass ejections and corotating interaction regions. *Space Weather*, *4*(9), 09004. <https://doi.org/10.1029/2005SW000211>
- Kilpua, E., Koskinen, H. E. J., & Pulkkinen, T. I. (2017). Coronal mass ejections and their sheath regions in interplanetary space. *Living Reviews in Solar Physics*, *14*(1), 5. <https://doi.org/10.1007/s41116-017-0009-6>
- Larson, D. E., Lillis, R. J., Lee, C. O., Dunn, P. A., Hatch, K., Robinson, M., et al. (2015). The MAVEN solar energetic particle investigation. *Space Science Reviews*, *195*(1–4), 153–172. <https://doi.org/10.1007/s11214-015-0218-z>
- Lee, C. O., Hara, T., Halekas, J. S., Thiemann, E., Chamberlin, P., Eparvier, F., et al. (2017). MAVEN observations of the solar cycle 24 space weather conditions at Mars. *Journal of Geophysical Research: Space Physics*, *122*(3), 2768–2794. <https://doi.org/10.1002/2016JA023495>
- Lee, C. O., Jakosky, B. M., Luhmann, J. G., Brain, D. A., Mays, M. L., Hassler, D. M., et al. (2018). Observations and impacts of the 10 September 2017 solar events at Mars: An overview and synthesis of the initial results. *Geophysical Research Letters*, *45*(17), 8871–8885. <https://doi.org/10.1029/2018GL079162>
- Lemen, J. R., Title, A. M., Akin, D. J., Boerner, P. F., Chou, C., Drake, J. F., et al. (2012). The atmospheric imaging assembly (AIA) on the solar dynamics observatory (SDO). *Solar Physics*, *275*(1–2), 17–40. <https://doi.org/10.1007/s11207-011-9776-8>

- Lepping, R. P., Acuña, M. H., Burlaga, L. F., Farrell, W. M., Slavin, J. A., Schatten, K. H., et al. (1995). The wind magnetic field investigation. *Space Science Reviews*, 71(1–4), 207–229. <https://doi.org/10.1007/BF00751330>
- Lin, R. P., Anderson, K. A., Ashford, S., Carlson, C., Curtis, D., Ergun, R., et al. (1995). A three-dimensional plasma and energetic particle investigation for the wind spacecraft. *Space Science Reviews*, 71(1–4), 125–153. <https://doi.org/10.1007/BF00751328>
- Lugaz, N., Farrugia, C. J., Smith, C. W., & Paulson, K. (2015). Shocks inside CMEs: A survey of properties from 1997 to 2006. *Journal of Geophysical Research: Space Physics*, 120(4), 2409–2427. <https://doi.org/10.1002/2014JA020848>
- Lugaz, N., Manchester, I., Ward, B., & Gombosi, T. I. (2005). Numerical simulation of the interaction of two coronal mass ejections from Sun to Earth. *The Astrophysical Journal*, 634(1), 651–662. <https://doi.org/10.1086/491782>
- Lugaz, N., Temmer, M., Wang, Y., & Farrugia, C. J. (2017). The interaction of successive coronal mass ejections: A review. *Solar Physics*, 292(4), 64. <https://doi.org/10.1007/s11207-017-1091-6>
- Luhmann, J. G., Dong, C. F., Ma, Y. J., Curry, S. M., Xu, S., Lee, C. O., et al. (2017). Martian magnetic storms. *Journal of Geophysical Research (Space Physics)*, 122(6), 6185–6209. <https://doi.org/10.1002/2016JA023513>
- Lynch, B. J. (2020). A model for coronal inflows and in/out pairs. *The Astrophysical Journal*, 905(2), 139. <https://doi.org/10.3847/1538-4357/abc5b3>
- Lynch, B. J., Antiochos, S. K., Li, Y., Luhmann, J. G., & DeVore, C. R. (2009). Rotation of coronal mass ejections during eruption. *The Astrophysical Journal*, 697(2), 1918–1927. <https://doi.org/10.1088/0004-637X/697/2/1918>
- Lynch, B. J., & Edmondson, J. K. (2013). Sympathetic magnetic breakout coronal mass ejections from pseudostreamers. *The Astrophysical Journal*, 764(1), 87. <https://doi.org/10.1088/0004-637X/764/1/87>
- Mavromichalaki, H., Papaioannou, A., Plainaki, C., Sarlanis, C., Souvatzoglou, G., Gerontidou, M., et al. (2011). Applications and usage of the real-time neutron monitor database. *Advances in Space Research*, 47(12), 2210–2222. <https://doi.org/10.1016/j.asr.2010.02.019>
- Mishra, S. K., & Srivastava, A. K. (2019). Linkage of geoeffective stealth CMEs associated with the eruption of coronal plasma channel and jet-like structure. *Solar Physics*, 294(12), 169. <https://doi.org/10.1007/s11207-019-1560-1>
- Mitchell, D. L., Mazelle, C., Sauvaud, J. A., Thocaven, J. J., Rouzaud, J., Fedorov, A., et al. (2016). The MAVEN solar wind electron analyzer. *Space Science Reviews*, 200(1–4), 495–528. <https://doi.org/10.1007/s11214-015-0232-1>
- Moro, J., Xu, J., Denardini, C. M., Resende, L. C. A., Da Silva, L. A., Chen, S. S., et al. (2022). Different sporadic-E (Es) layer types development during the August 2018 geomagnetic storm: Evidence of auroral type (es_a) over the SAMA region. *Journal of Geophysical Research: Space Physics*, 127(2), e2021JA029701. <https://doi.org/10.1029/2021JA029701>
- Müller, D., Nicula, B., Felix, S., Verstringe, F., Bourgoignie, B., Csillaghy, A., et al. (2017). JHelioviewer: Time-dependent 3D visualisation of solar and heliospheric data. *Astronomy & Astrophysics*, 606, A10. <https://doi.org/10.1051/0004-6361/201730893>
- Mulligan, T., Russell, C. T., & Luhmann, J. G. (1998). Solar cycle evolution of the structure of magnetic clouds in the inner heliosphere. *Geophysical Research Letters*, 25(15), 2959–2962. <https://doi.org/10.1029/98GL01302>
- Nieves-Chinchilla, T., Linton, M. G., Hidalgo, M. A., & Vourlidis, A. (2018). Elliptic-cylindrical analytical flux rope model for magnetic clouds. *The Astrophysical Journal*, 861(2), 139. <https://doi.org/10.3847/1538-4357/aac951>
- Nitta, N. V. (2011). Observables indicating two major coronal mass ejections during the WHI. *Solar Physics*, 274(1–2), 219–232. <https://doi.org/10.1007/s11207-011-9806-6>
- Nitta, N. V., & Mulligan, T. (2017). Earth-Affecting coronal mass ejections without obvious low coronal signatures. *Solar Physics*, 292(9), 125. <https://doi.org/10.1007/s11207-017-1147-7>
- Nitta, N. V., Mulligan, T., Kilpua, E. K. J., Lynch, B. J., Mierla, M., O’Kane, J., et al. (2021). Understanding the origins of problem geomagnetic storms associated with “stealth” coronal mass ejections. *Space Science Reviews*, 217(8), 82. <https://doi.org/10.1007/s11214-021-00857-0>
- O’Dwyer, B., Del Zanna, G., Mason, H. E., Weber, M. A., & Tripathi, D. (2010). SDO/AIA response to coronal hole, quiet Sun, active region, and flare plasma. *Astronomy & Astrophysics*, 521, A21. <https://doi.org/10.1051/0004-6361/201014872>
- Odstrcil, D. (2003). Modeling 3-D solar wind structure. *Advances in Space Research*, 32(4), 497–506. [https://doi.org/10.1016/S0273-1177\(03\)00332-6](https://doi.org/10.1016/S0273-1177(03)00332-6)
- Odstrcil, D., Riley, P., & Zhao, X. P. (2004). Numerical simulation of the 12 May 1997 interplanetary CME event. *Journal of Geophysical Research*, 109(A2), A02116. <https://doi.org/10.1029/2003JA010135>
- Ogilvie, K. W., Chornay, D. J., Fritzenreiter, R. J., Hunsaker, F., Keller, J., Lobell, J., et al. (1995). SWE, A comprehensive plasma instrument for the wind spacecraft. *Space Science Reviews*, 71(1–4), 55–77. <https://doi.org/10.1007/BF00751326>
- Ogilvie, K. W., & Desch, M. D. (1997). The wind spacecraft and its early scientific results. *Advances in Space Research*, 20(4–5), 559–568. [https://doi.org/10.1016/S0273-1177\(97\)00439-0](https://doi.org/10.1016/S0273-1177(97)00439-0)
- Opgenoorth, H. J., Andrews, D. J., Fränz, M., Lester, M., Edberg, N. J. T., Morgan, D., et al. (2013). Mars ionospheric response to solar wind variability. *Journal of Geophysical Research: Space Physics*, 118(10), 6558–6587. <https://doi.org/10.1002/jgra.50537>
- Owens, M. J. (2006). Magnetic cloud distortion resulting from propagation through a structured solar wind: Models and observations. *Journal of Geophysical Research*, 111(A12), A12109. <https://doi.org/10.1029/2006JA011903>
- Palmerio, E., Kilpua, E. K. J., James, A. W., Green, L. M., Pomoell, J., Isavnin, A., & Valori, G. (2017). Determining the intrinsic CME flux rope type using remote-sensing solar disk observations. *Solar Physics*, 292(2), 39. <https://doi.org/10.1007/s11207-017-1063-x>
- Palmerio, E., Scolini, C., Barnes, D., Magdalenic, J., West, M. J., Zhukov, A. N., et al. (2019). Multipoint Study of Successive Coronal Mass Ejections Driving Moderate Disturbances at 1 au. *The Astrophysical Journal*, 878(1), 37. <https://doi.org/10.3847/1538-4357/ab1850>
- Pesnell, W. D., Thompson, B. J., & Chamberlin, P. C. (2012). The solar dynamics observatory (SDO). *Solar Physics*, 275(3–15), 3–15. <https://doi.org/10.1007/s11207-011-9841-3>
- Piersanti, M., De Michelis, P., Del Moro, D., Tozzi, R., Pezzopane, M., Consolini, G., et al. (2020). From the Sun to Earth: Effects of the 25 August 2018 geomagnetic storm. *Annales Geophysicae*, 38(3), 703–724. <https://doi.org/10.5194/angeo-38-703-2020>
- Pulkkinen, T. (2007). Space weather: Terrestrial perspective. *Living Reviews in Solar Physics*, 4, 1. <https://doi.org/10.12942/lrsp-2007-1>
- Reinard, A. A., & Biesecker, D. A. (2009). The relationship between coronal dimming and coronal mass ejection properties. *The Astrophysical Journal*, 705(1), 914–919. <https://doi.org/10.1088/0004-637X/705/1/914>
- Reiss, M. A., Muglach, K., Mullinix, R., Kuznetsova, M. M., Wiegand, C., Temmer, M., & ISWAT H1-01 Team Members. (2022). Unifying the validation of ambient solar wind models. *Advances in Space Research*. <https://doi.org/10.1016/j.asr.2022.05.026>
- Richardson, I. G. (2004). Energetic particles and corotating interaction regions in the solar wind. *Space Science Reviews*, 111(3), 267–376. <https://doi.org/10.1023/B:SPAC.0000032689.52830.3e>
- Richardson, I. G. (2018). Solar wind stream interaction regions throughout the heliosphere. *Living Reviews in Solar Physics*, 15, 1. <https://doi.org/10.1007/s41116-017-0011-z>
- Richardson, I. G., Cliver, E. W., & Cane, H. V. (2001). Sources of geomagnetic storms for solar minimum and maximum conditions during 1972–2000. *Geophysical Research Letters*, 28(13), 2569–2572. <https://doi.org/10.1029/2001GL013052>

- Richardson, I. G., Webb, D. F., Zhang, J., Berdichevsky, D. B., Biesecker, D. A., Kasper, J. C., et al. (2006). Major geomagnetic storms ($Dst \leq -100$ nT) generated by corotating interaction regions. *Journal of Geophysical Research*, *111*(A7), A07S09. <https://doi.org/10.1029/2005JA011476>
- Riley, P., Caplan, R. M., Downs, C., Linker, J. A., & Lionello, R. (2022). Comparing and contrasting the properties of the inner heliosphere for the three most recent solar minima. *Journal of Geophysical Research: Space Physics*, *127*(8), e2022JA030261. <https://doi.org/10.1029/2022JA030261>
- Riley, P., & Crooker, N. U. (2004). Kinematic Treatment of coronal mass ejection evolution in the solar wind. *The Astrophysical Journal*, *600*(2), 1035–1042. <https://doi.org/10.1086/379974>
- Riley, P., Linker, J. A., Lionello, R., & Mikic, Z. (2012). Corotating interaction regions during the recent solar minimum: The power and limitations of global MHD modeling. *Journal of Atmospheric and Solar-Terrestrial Physics*, *83*, 1–10. <https://doi.org/10.1016/j.jastp.2011.12.013>
- Riley, P., Linker, J. A., & Mikić, Z. (2001). An empirically-driven global MHD model of the solar corona and inner heliosphere. *Journal of Geophysical Research*, *106*(A8), 15889–15902. <https://doi.org/10.1029/2000JA000121>
- Sánchez-Cano, B., Hall, B. E. S., Lester, M., Mays, M. L., Witasse, O., Ambrosi, R., et al. (2017). Mars plasma system response to solar wind disturbances during solar minimum. *Journal of Geophysical Research: Space Physics*, *122*(6), 6611–6634. <https://doi.org/10.1002/2016JA023587>
- Sánchez-Cano, B., Lester, M., Andrews, D. J., Opgenoorth, H., Lillis, R., Leblanc, F., et al. (2021). Mars' plasma system. Scientific potential of coordinated multipoint missions: “The next generation”. *Experimental Astronomy*. <https://doi.org/10.1007/s10686-021-09790-0>
- Scolini, C., Chané, E., Temmer, M., Kilpua, E. K. J., Dissauer, K., Veronig, A. M., et al. (2020). CME-CME interactions as sources of CME geoeffectiveness: The formation of the complex ejecta and intense geomagnetic storm in 2017 early september. *The Astrophysical Journal: Supplement Series*, *247*(1), 21. <https://doi.org/10.3847/1538-4365/ab6216>
- Spence, H. E., Case, A. W., Golightly, M. J., Heine, T., Larsen, B. A., Blake, J. B., et al. (2010). CRaTER: The cosmic ray Telescope for the effects of radiation experiment on the lunar reconnaissance orbiter mission. *Space Science Reviews*, *150*(1–4), 243–284. <https://doi.org/10.1007/s11214-009-9584-8>
- Stone, E. C., Frandsen, A. M., Mewaldt, R. A., Christian, E. R., Margolies, D., Ormes, J. F., & Snow, F. (1998). The advanced composition explorer. *Space Science Reviews*, *86*(1/4), 1–22. <https://doi.org/10.1023/A:1005082526237>
- Temmer, M., & Nitta, N. V. (2015). Interplanetary propagation behavior of the fast coronal mass ejection on 23 July 2012. *Solar Physics*, *290*(3), 919–932. <https://doi.org/10.1007/s11207-014-0642-3>
- Thampi, S. V., Krishnaprasad, C., Nampoothiri, G. G., & Pant, T. K. (2021). The impact of a stealth CME on the Martian topside ionosphere. *Monthly Notices of the Royal Astronomical Society*, *503*(1), 625–632. <https://doi.org/10.1093/mnras/stab494>
- Thernisien, A. (2011). Implementation of the graduated cylindrical shell model for the three-dimensional reconstruction of coronal mass ejections. *The Astrophysical Journal: Supplement Series*, *194*(2), 33. <https://doi.org/10.1088/0067-0049/194/2/33>
- Thernisien, A., Vourlidas, A., & Howard, R. A. (2009). Forward modeling of coronal mass ejections using STEREO/SECCHI data. *Solar Physics*, *256*(1–2), 111–130. <https://doi.org/10.1007/s11207-009-9346-5>
- Thernisien, A. F. R., Howard, R. A., & Vourlidas, A. (2006). Modeling of flux rope coronal mass ejections. *The Astrophysical Journal*, *652*(1), 763–773. <https://doi.org/10.1086/508254>
- The SunPy Community, Barnes, W. T., Bobra, M. G., Christe, S. D., Freij, N., Hayes, L. A., et al. (2020). The SunPy project: Open source development and status of the version 1.0 core package. *The Astrophysical Journal*, *890*(1), 68. <https://doi.org/10.3847/1538-4357/ab4f7a>
- Thompson, B. J., Cliver, E. W., Nitta, N., Delannée, C., & Delaboudinière, J.-P. (2000). Coronal dimmings and energetic CMEs in April–May 1998. *Geophysical Research Letters*, *27*(10), 1431–1434. <https://doi.org/10.1029/1999GL003668>
- Thompson, B. J., Gibson, S. E., Schroeder, P. C., Webb, D. F., Arge, C. N., Bisi, M. M., et al. (2011). A snapshot of the Sun near solar minimum: The whole heliosphere interval. *Solar Physics*, *274*(1–2), 29–56. <https://doi.org/10.1007/s11207-011-9891-6>
- Titov, V. S., Mikic, Z., Linker, J. A., & Lionello, R. (2008). 1997 May 12 coronal mass ejection event. I. A simplified model of the preeruptive magnetic structure. *The Astrophysical Journal*, *675*(2), 1614–1628. <https://doi.org/10.1086/527280>
- Török, T., Panasenco, O., Titov, V. S., Mikić, Z., Reeves, K. K., Velli, M., et al. (2011). A model for magnetically coupled sympathetic eruptions. *The Astrophysical Journal Letters*, *739*(2), L63. <https://doi.org/10.1088/2041-8205/739/2/L63>
- von Steiger, R., & Richardson, J. D. (2006). ICMEs in the outer heliosphere and at high latitudes: An introduction. *Space Science Reviews*, *123*(1–3), 111–126. <https://doi.org/10.1007/s11214-006-9015-z>
- Vourlidas, A., Balmaceda, L. A., Stenborg, G., & Dal Lago, A. (2017). Multi-viewpoint coronal mass ejection catalog based on STEREO COR2 observations. *The Astrophysical Journal*, *838*(2), 141. <https://doi.org/10.3847/1538-4357/aa67f0>
- Vourlidas, A., Lynch, B. J., Howard, R. A., & Li, Y. (2013). How many CMEs have flux ropes? Deciphering the signatures of shocks, flux ropes, and prominences in coronagraph observations of CMEs. *Solar Physics*, *284*, 179–201. <https://doi.org/10.1007/s11207-012-0084-8>
- Vourlidas, A., & Webb, D. F. (2018). Streamer-blowout coronal mass ejections: Their properties and relation to the coronal magnetic field structure. *The Astrophysical Journal*, *861*(2), 103. <https://doi.org/10.3847/1538-4357/aaca3e>
- Wang, Y. M., Sheeley, N. R., Socker, D. G., Howard, R. A., & Rich, N. B. (2000). The dynamical nature of coronal streamers. *Journal of Geophysical Research*, *105*(A11), 25133–25142. <https://doi.org/10.1029/2000JA000149>
- Wang, Y. M., Ye, P. Z., & Wang, S. (2003). Multiple magnetic clouds: Several examples during March–April 2001. *Journal of Geophysical Research*, *108*(A10), 1370. <https://doi.org/10.1029/2003JA009850>
- Webb, D. F., & Howard, T. A. (2012). Coronal mass ejections: Observations. *Living Reviews in Solar Physics*, *9*(1), 3. <https://doi.org/10.12942/lrsp-2012-3>
- Winslow, R. M., Lugaz, N., Scolini, C., & Galvin, A. B. (2021). First simultaneous in situ measurements of a coronal mass ejection by parker solar probe and STEREO-A. *The Astrophysical Journal*, *916*(2), 94. <https://doi.org/10.3847/1538-4357/ac0821>
- Younas, W., Amory-Mazaudier, C., Khan, M., & Fleury, R. (2020). Ionospheric and magnetic signatures of a space weather event on 25–29 August 2018: CME and HSSWs. *Journal of Geophysical Research: Space Physics*, *125*(8), e2020JA027981. <https://doi.org/10.1029/2020JA027981>
- Zhang, J., Richardson, I. G., Webb, D. F., Gopalswamy, N., Huttunen, E., Kasper, J. C., et al. (2007). Solar and interplanetary sources of major geomagnetic storms ($Dst \leq -100$ nT) during 1996–2005. *Journal of Geophysical Research*, *112*(A10), A10102. <https://doi.org/10.1029/2007JA012321>
- Zhang, Z., Chen, L., Liu, S., Xiong, Y., Li, X., Wang, Y., et al. (2020). Chorus acceleration of relativistic electrons in extremely low L-shell during geomagnetic storm of August 2018. *Geophysical Research Letters*, *47*(4), e2019GL086226. <https://doi.org/10.1029/2019GL086226>
- Zhao, D., Guo, J., Huang, H., Lin, H., Hong, Y., Feng, X., et al. (2021). Interplanetary coronal mass ejections from MAVEN orbital observations at Mars. *The Astrophysical Journal*, *923*(1), 4. <https://doi.org/10.3847/1538-4357/ac294b>
- Zurbuchen, T. H., & Richardson, I. G. (2006). In-situ solar wind and magnetic field signatures of interplanetary coronal mass ejections. *Space Science Reviews*, *123*(1–3), 31–43. <https://doi.org/10.1007/s11214-006-9010-4>